

A Hybrid Approach for Characterizing Linear and Nonlinear Electromagnetic Scattering: Theory and Applications

by DaHan Liao

ARL-TR-6261

November 2012

NOTICES

Disclaimers

The findings in this report are not to be construed as an official Department of the Army position unless so designated by other authorized documents.

Citation of manufacturer's or trade names does not constitute an official endorsement or approval of the use thereof.

Destroy this report when it is no longer needed. Do not return it to the originator.

Army Research Laboratory

Adelphi, MD 20783-1197

ARL-TR-6261

November 2012

A Hybrid Approach for Characterizing Linear and Nonlinear Electromagnetic Scattering: Theory and Applications

DaHan Liao

Sensors and Electron Devices Directorate, ARL

REPORT DOCUMENTATION PAGE			Form Approved OMB No. 0704-0188		
Public reporting burden for this collection of information is estimated to average 1 hour per response, including the time for reviewing instructions, searching existing data sources, gathering and maintaining the data needed, and completing and reviewing the collection information. Send comments regarding this burden estimate or any other aspect of this collection of information, including suggestions for reducing the burden, to Department of Defense, Washington Headquarters Services, Directorate for Information Operations and Reports (0704-0188), 1215 Jefferson Davis Highway, Suite 1204, Arlington, VA 22202-4302. Respondents should be aware that notwithstanding any other provision of law, no person shall be subject to any penalty for failing to comply with a collection of information if it does not display a currently valid OMB control number. PLEASE DO NOT RETURN YOUR FORM TO THE ABOVE ADDRESS.					
1. REPORT DATE (DD-MM-YYYY) November 2012		2. REPORT TYPE Final		3. DATES COVERED (From - To) 2011–2012	
4. TITLE AND SUBTITLE A Hybrid Approach for Characterizing Linear and Nonlinear Electromagnetic Scattering: Theory and Applications			5a. CONTRACT NUMBER		
			5b. GRANT NUMBER		
			5c. PROGRAM ELEMENT NUMBER 1NE4II		
6. AUTHOR(S) DaHan Liao			5d. PROJECT NUMBER		
			5e. TASK NUMBER		
			5f. WORK UNIT NUMBER		
7. PERFORMING ORGANIZATION NAME(S) AND ADDRESS(ES) U.S. Army Research Laboratory ATTN: RDRL-SER-U 2800 Powder Mill Road Adelphi MD 20783-1197			8. PERFORMING ORGANIZATION REPORT NUMBER ARL-TR-6261		
9. SPONSORING/MONITORING AGENCY NAME(S) AND ADDRESS(ES)			10. SPONSOR/MONITOR'S ACRONYM(S)		
			11. SPONSOR/MONITOR'S REPORT NUMBER(S)		
12. DISTRIBUTION/AVAILABILITY STATEMENT Approved for public release; distribution unlimited.					
13. SUPPLEMENTARY NOTES					
14. ABSTRACT A hybrid physics-based solver is developed for studying the harmonic scattering of circuit-component-loaded objects. The proposed approach features a combination of three-dimensional (3-D) electromagnetic field simulations—of both the full-wave and the asymptotic types—in the propagation and radio frequency (RF) component domains, and Simulation Program with Integrated Circuit Emphasis (SPICE) simulations in the circuit domain. In effect, a systematic framework is established for attaining generalized approximate solutions of the multiscale harmonic radar scattering problem. The solver is applied for analyzing the conventional (linear) and nonlinear scattering components from an RF circuit-loaded object placed in near-ground and through-wall settings: the scattering responses as functions of incident power, standoff distance, and azimuth angle are considered; the localization of the scatterer using both the linear and the nonlinear returns is also demonstrated by exploiting a subspace-based time-reversal method.					
15. SUBJECT TERMS Computational electromagnetics, hybrid simulation method, linear and nonlinear scattering, time-reversal MUSIC imaging					
16. SECURITY CLASSIFICATION OF:			17. LIMITATION OF ABSTRACT UU	18. NUMBER OF PAGES 62	19a. NAME OF RESPONSIBLE PERSON DaHan Liao
a. REPORT Unclassified	b. ABSTRACT Unclassified	c. THIS PAGE Unclassified			19b. TELEPHONE NUMBER (Include area code) (301) 394-1741

Contents

List of Figures	iv
1. Introduction	1
2. Formulation of Hybrid Simulation Framework	3
2.1 Electromagnetic Solver	5
2.1.1 MPIE-MoM	5
2.1.2 Approximation for Green's Functions	6
2.2 Wideband Lumped-element Equivalent Circuit Synthesis	7
2.3 Circuit Simulation	8
2.4 Electromagnetic Field Propagator	8
3. Numerical Examples: Applications of the Hybrid Solver	9
3.1 Circuit-Component-Loaded Scatterer in Half-space Environment	9
3.2 Circuit-Component-Loaded Scatterer in Room Environment.....	18
4. Conclusions	23
5. References	25
Appendix A. Higher-Order Asymptotic Evaluation of Near-Earth Wave Propagation Characteristics of Electric Current Sources	31
Appendix B. Sommerfeld Integrals for Electric Current Sources	41
Appendix C. Traveling-Wave Amplifier Design	45
List of Symbols, Abbreviations, and Acronyms	53
Distribution List	54

List of Figures

Figure 1. Standoff sensing of circuit-component-loaded scatterer buried in the ground.	2
Figure 2. Standoff, through-wall sensing of circuit-component-loaded scatterer. (A flat roof structure is assumed but not shown.)	3
Figure 3. Framework of hybrid solver.	4
Figure 4. Antenna and filter for RF front-end: (a) top view; (b) bottom view; and (c) side view. $\epsilon_{r1} = \epsilon_{r2} = 4.5$ ($\tan\delta \approx 0.04$); the thickness of each substrate is 1.6 mm. The distributed filter has dimensions $\sim 10.7 \text{ cm} \times 7 \text{ cm}$; the radius of the circular patch antenna is 1.79 cm, and the length of the slot is 1.14 cm.	11
Figure 5. Effective capacitance of varactor used in the setup shown in figure 4 as function of DC bias voltage.	12
Figure 6. $ S_{11} $ for the dual-band, slot-loaded circular patch antenna as function of frequency and varactor capacitance.	12
Figure 7. S -parameters for microstrip dual-band bandpass filter as function of frequency.	13
Figure 8. Backscattered response of scatterer in figure 4 at fundamental and second harmonic for two levels of transmitted power. The noise floor (kT) shown is at -173.8 dBm/Hz	14
Figure 9. Variation of scattered electric field components as a function of azimuth angle.	14
Figure 10. Backscattered response as a function of range: (a) f_o and (b) $2f_o$	15
Figure 11. Backscattered responses at fundamental, second, and third harmonics of scatterer in figure 4 connected to a traveling-wave amplifier.	16
Figure 12. Imaging results for a buried target scenario: (a) Scene containing target and clutter, (b) image generated using scattering response at $f_o = 840 \text{ MHz}$ (both the target and clutter are imaged), and (c) image generated using scattering response at $2f_o = 1680 \text{ MHz}$ (only the target is captured).	18
Figure 13. Backscattered response of scenario shown in figure 2: (a) without and (b) with circuit-component-loaded scatterer in room.	20
Figure 14. Backscattered response at fundamental and second harmonic as function of azimuth angle for scenario in figure 2.	21
Figure 15. Simulated vs. measured responses for propagation in presence of a wall.	22
Figure 16. Simulated vs. measured responses for propagation in presence of a wall.	23
Figure A-1. (a) Magnitude and (b) phase of the electric fields of a horizontal electric dipole as a function of range. The dipole is located on the z -axis at a 2-m height above the ground and the observation point is at a 1.7-m height along a radial line at $\phi = 30^\circ$. Ground properties: $\epsilon_r = 4$, $\sigma_d = 10 \text{ mS/m}$, and $f = 300 \text{ MHz}$	39

Figure A-2. (a) Magnitude and (b) phase of the electric fields of a horizontal electric dipole as a function of range. The dipole is buried in the ground at a 10-cm depth and the observation point is at a 1.7-m height along a radial line at $\phi = 30^\circ$. Ground properties: $\epsilon_r' = 4$, $\sigma_d = 10$ mS/m, and $f = 300$ MHz.	40
Figure C-1. TriQuint small-signal model for transistor.	45
Figure C-2. Simulation with simplified small-signal model.	46
Figure C-3. Comparison between full small-signal model (blue lines) and simplified small-signal model (red lines).	47
Figure C-4. Design curves.	48
Figure C-5. Line termination.	49
Figure C-6. (a) An example layout for $n = 2$ using lumped-elements, (b) component values, and (c) simulation results of lumped-element-based design.	50
Figure C-7. Schematic and gain simulation for preliminary design with $n = 2$	51

INTENTIONALLY LEFT BLANK.

1. Introduction

The characterization of the harmonic scattering response of circuit-component-loaded scatterers is an important problem in both sensing and electromagnetic interference applications. A circuit-component-loaded scatterer is defined herein as a scatterer that contains circuit lumped-elements (e.g., resistors, inductors, capacitors) and/or radio frequency (RF) components (e.g., transmission lines, antennas, distributed filters, amplifiers) within its structure. In contrast to the standard radar scattering problem, which necessitates the analysis of the radio responses of objects solely based on their dielectric compositions and physical geometries—and which has been thoroughly treated by numerous studies, the *generalized* scattering characterization of circuit-component-loaded objects has thus far garnered relatively less attention in open literature—the interesting applications to which this research area can be applied notwithstanding. From the sensing perspective, a circuit-component-loaded scatterer—when properly excited—could potentially re-radiate unique features, enabling it to be differentiated from an ordinary scatterer: for example, the antenna and filter at the front-end of an RF device can modulate the radar backscattering response, facilitating opportunities for classification and detection; the nonlinear components within the scatterer can also generate harmonic signals and re-emission, which can be exploited to extract the object embedded in linear clutter. As related to the design of communication systems, circuit-element modulated scattering plays a role in understanding how inter-coupling effects among different radios influence transceiver performance and signal fidelity. In all the aforementioned applications, an end-to-end (or transmitter terminal-to-receiver terminal), system-level simulation capability is needed to attain a fundamental understanding of the signal interactions. Accordingly, in this study, a systematic strategy for analyzing the linear and nonlinear responses of the circuit-component-loaded scatterer is developed, with specific relevance to active RF sensing, detection, and localization.

The formidable scope of the current problem inherently spans both the electromagnetic and circuit domains, and a full-wave analysis strategy must track the signals or waves across a multiscale simulation domain consisting of effects occurring at the propagation, RF component, and circuit levels. As shown in figures 1 and 2, in the *external* problem, the propagation and scattering interactions of the radiation (or current) sources with the environment determine the incident fields at the scatterer as well as the re-radiated fields subsequently received at the receiver. In the *internal* problem, the coupling of energy into the scatterer and the generation of harmonics are complicated functions of the circuit elements and RF components. Full-wave electromagnetic solvers—for instance, the method-of-moments (MoM) and finite-difference time-domain (FDTD)—can be used to characterize RF components such as antennas and distributed filters. The treatment of active, passive, linear, and nonlinear lumped-elements also has been considered in the FDTD framework (1–4). In reference 5, a harmonic balance procedure—in conjunction with MoM—is proposed to analyze the radar cross section of simple

wire scatterers with nonlinear loads. To predict the microwave nonlinear behaviors of high temperature superconducting filters, an iterative MoM approach is developed in reference 6: the linear response is calculated in the frequency domain using the electric field integral equation and the nonlinear one is solved in the time domain. Works of direct relevance to RF transceiver design also have been undertaken by various researchers: the scattering of antennas connected to nonlinear loads is addressed in 7–17; harmonic generation by reactively-tunable antennas is investigated via a full-wave approach in 18 as well as a mixture of full-wave and equivalent-circuit methods in 19. As related to electromagnetic inference and compatibility studies, the prediction of emissions from printed circuit boards (PCBs) using numerical methods (e.g., partial element equivalent circuit method, finite integration technique, FDTD) has been discussed in works by, for example, 20–23—albeit the focus of these studies is not on nonlinear effects. As alluded to above, although there exists a panoply of works—in both the electromagnetic and circuit domains—that are potentially applicable, either directly or indirectly, to the treatment of loaded scatterers, a complete system-level analysis of the harmonic scattering problem—that is, the tracing of the signal interaction from the transmitter terminal, across an environment, into an RF circuit network, and back to the receiver—has not been considered in detail.

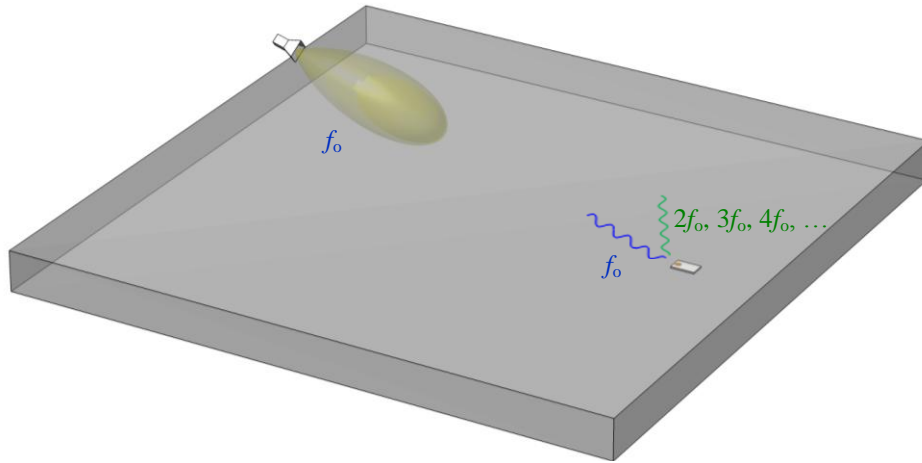


Figure 1. Standoff sensing of circuit-component-loaded scatterer buried in the ground.

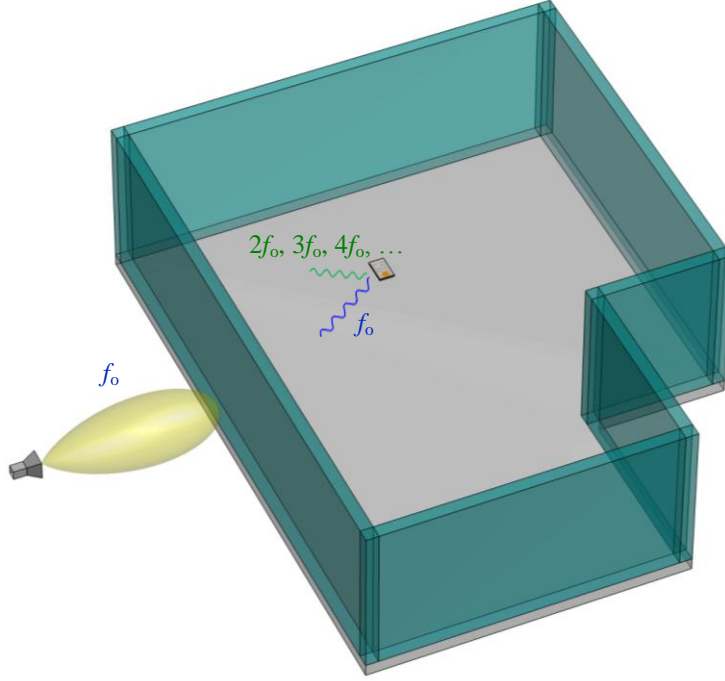


Figure 2. Standoff, through-wall sensing of circuit-component-loaded scatterer.
(A flat roof structure is assumed but not shown.)

In view of the current lack of a comprehensive, generalized solver for studying the stated multiscale radar scattering effects, a hybrid simulation approach is presented in this work—with an emphasis on the characterization of the scattering properties of circuit-component-loaded scatterers in complex environments. The framework of the analysis involves a combination of electromagnetic and circuit simulations: the linear (or ordinary) response is determined in the electromagnetic domain, whereas the nonlinear response is deduced by computing the currents and voltages of an equivalent circuit network in a Simulation Program with Integrated Circuit Emphasis (SPICE) solver, and the interaction of the electromagnetic fields at the propagation level is characterized by asymptotic techniques. The study is organized as follows: in section 2, the development of the individual components of the simulation framework is detailed; in section 3, the application of the solver is illustrated for two practical scenarios of interest—viz., in the first case, the scatterer is in the presence of a dielectric ground; in the second case, the scatterer is in a room environment; and in section 4, a summary of the work is presented.

2. Formulation of Hybrid Simulation Framework

The linear and nonlinear responses of a circuit-component-loaded structure (excited by a time-harmonic field) are calculated with a solution approach encompassing both the electromagnetic and circuit domains. As depicted in figure 3, the solver is separable into the following five steps:

1. The S -parameters and the current densities of the individual RF components (antennas, distributed filters, PCB structure, etc.) are characterized using a full-wave approach—in this case, a MoM solver is employed. The initial incident field at the scatterer is deduced by applying an asymptotic field propagator to the radiation source (or transmitting antenna). Note that to accomplish this step, the nonlinear circuit elements first have to be extracted from the circuit, and—for the calculation of the current densities—the RF components must be terminated with appropriate loads as determined by the actual circuit layout.
2. Using the electromagnetic simulation results, wideband equivalent circuit sub-networks are synthesized for the RF components. These equivalent sub-networks are combined with the extracted nonlinear components (and other lumped and discrete elements) from the original circuit layout to form an overall equivalent network representation for the RF structure.
3. The stimulus (voltage or current source) for the derived equivalent network is calculated based on the linear electromagnetic response of the scatterer.
4. The equivalent network is placed in a SPICE solver, and simulation is performed to obtain the effective radiated power at all the harmonics of interest.
5. Finally, the re-radiation for each spectral component is propagated to the receiver location using asymptotic routines. It should be mentioned that the first-order solution (for the fundamental frequency scattering response) can be approximated by applying steps 1 and 5 only—specifically, a linear MoM approach can be used to simulate the entire RF structure, with the discrete circuit elements appearing only as equivalent impedance loads at the structure ports.

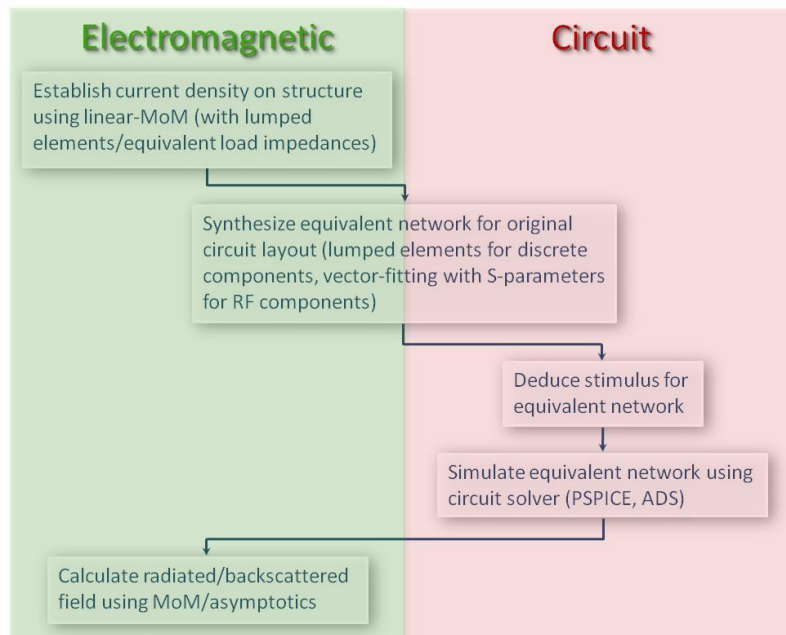


Figure 3. Framework of hybrid solver.

The development of the major components of the simulation methodology is discussed below.

2.1 Electromagnetic Solver

The linear MoM algorithm for calculating the RF response of a structure is based on an approach originally established by Liao (24) for analyzing grounded antenna performance. The details of the electromagnetic solver are described below; for further explanations, the interested reader is referred to references 24 and 25.

2.1.1 MPIE-MoM

To calculate the radiating and induced currents of the RF structure, a MoM procedure is solved through the use of a standard form of the electric field integral equation. For an arbitrary field impinging upon a perfectly conducting structure, the mixed potential integral equation (MPIE), in terms of vector potential \vec{A} and scalar potential Φ , is given by the following:

$$\hat{n} \times [\vec{E}_{inc}(\vec{r}) + \vec{E}_{scat}(\vec{r})] = 0, \quad \vec{r} \in \text{structure surface } s; \quad (1)$$

$$\vec{E}_{scat}(\vec{r}) = -j\omega\vec{A}(\vec{r}) - \nabla\Phi(\vec{r}); \quad (2)$$

where

$$\vec{A}(\vec{r}) = \int_s \vec{G}^A(\vec{r}, \vec{r}') \cdot \vec{J}_s(\vec{r}') d\vec{r}'; \quad (3)$$

$$\Phi(\vec{r}) = -\frac{1}{j\omega} \int_s G^\Phi(\vec{r}, \vec{r}') \nabla' \cdot \vec{J}_s(\vec{r}') d\vec{r}'. \quad (4)$$

The dyadic and scalar Green's functions have been derived (26–28) for the case when the region of interest is, for example, the upper medium of a half-space:

$$\vec{G}^A(\vec{r}, \vec{r}') = \frac{\mu_o}{4\pi} \left\{ g_{fs} \vec{I} + \begin{bmatrix} 0 & 0 & g_{xz} \\ 0 & 0 & g_{yz} \\ -g_{xz} & -g_{yz} & -2Kg_i \end{bmatrix} + \begin{bmatrix} I_{xx} & 0 & I_{xz} \\ 0 & I_{xx} & I_{yz} \\ -I_{xz} & -I_{yz} & I_{zz} \end{bmatrix} \right\}; \quad (5)$$

$$G^\Phi(\vec{r}, \vec{r}') = \frac{1}{4\pi\epsilon_o} \{ g_{fs} + Kg_i + I_\Phi \}; \quad (6)$$

where \vec{I} is the unity matrix and

$$g_{fs,i} = \frac{e^{-jk_o R_{fs,i}}}{R_{fs,i}}; \quad (7)$$

$$g_{xz} = -K \cos \phi \left[\frac{1}{\rho} e^{-jk_o(z+z')} - \frac{(z+z')}{\rho} g_i \right]; \quad (8)$$

$$g_{yz} = -K \sin \phi \left[\frac{1}{\rho} e^{-jk_o(z+z')} - \frac{(z+z')}{\rho} g_i \right]; \quad (9)$$

$$R_{fs} = \sqrt{\rho^2 + (z-z')^2}; \quad R_i = \sqrt{\rho^2 + (z+z')^2}; \quad K = \frac{1 - \epsilon_{rg}}{1 + \epsilon_{rg}}. \quad (10)$$

In the above expressions, the quantities denoted by subscripts “*fs*” and “*i*” correspond to free space and image components, respectively. The Sommerfeld integrals (*I*’s) needed to complete equations 5 and 6 are defined in references 24 and 25. A set of expressions similar to equations 5–10 can be derived for the case when the region of interest is the lower medium of the half-space, or when the propagation background is a multi-layered (horizontally stratified) medium.

After meshing the structure of interest with triangular facets, by expanding the unknown surface current density \vec{j}_s as a summation of Rao-Wilton-Glisson basis functions (29, 30) and then testing equation 1 with the same type of functions, a matrix equation is formed, enabling the calculation of the surface current distribution throughout the structure. A procedure similar to the one shown in reference 29 can be used for setting up the matrix equation; and, with the introduction of normalized area coordinates, the face-pair combination evaluation can be implemented to speed up the impedance matrix filling process by eliminating redundant computational routines inherent in the edge-pair combination evaluation. For a voltage-source excited structure, a delta-gap model is assumed for the excitation vector in the matrix equation; in this model, an incident field only exists over the triangular patches spanning the gap location. For a more general incident field, the value of the incident field is assumed to be constant over each patch and equal to its value at the patch’s centroid.

2.1.2 Approximation for Green’s Functions

Note that two primary difficulties are encountered when calculating the impedance matrix elements using equations 5 and 6. One is due to the singularities that would emerge in the expressions g_{fs} , g_i , g_{xz} , and g_{yz} for certain impedance elements; however, singularity extraction techniques have been used successfully in obtaining closed-form solutions to the so-called self-terms (31–33). Also, a quadrature routine can be employed in computing the elements containing g_{xz} and g_{yz} , even in the presence of singularities. The second difficulty concerns the calculation of the impedance matrix elements in the presence of the Sommerfeld integrals. Implementing an exact routine to calculate the impedance matrix elements would necessitate the evaluation of a triple integral. To expedite the matrix filling process, different common schemes are available in efficiently calculating the Sommerfeld integrals—either by speeding up the convergence rate of the integrals or approximating the integrals with closed-form expressions. Since the Sommerfeld integrals are slowly convergent (especially for small $(z+z')$) along the original path on the real-axis, a deformed path (e.g., steepest descent path) can be exploited to achieve faster convergence. To avoid repeated calculation of the same integrals, another class of methods uses

a pre-compute/tabulate/interpolate routine in which the values of the integrals at a finite number of sampled spatial locations are calculated in advance (using convergence acceleration techniques) and then are stored in a database to serve as a base set for interpolation by the MoM procedure. In this study, the method of discrete complex images is employed to approximate all the Sommerfeld integrals with closed-form analytical expressions; thus, by eliminating the innermost of the triple integral, the remaining double integral can be carried out readily using a standard quadrature algorithm. After mapping the integrands as a sum of N exponentials of the form $\sum_{v=1}^N \alpha_v e^{-jk_{oz}\beta_v}$ on the complex k_{oz} -plane using the generalized pencil of function method (34–37), either of the following two identities is applied in approximating the resulting simplified Sommerfeld integrals in canonical forms:

$$\int_0^\infty \frac{1}{jk_{oz}} e^{-jk_{oz}(z+z')} J_0(k_\rho \rho) k_\rho dk_\rho = \frac{e^{-jk_o R_i}}{R_i}; \quad (11)$$

$$\int_0^\infty e^{-jk_{oz}(z+z')} J_1(k_\rho \rho) k_\rho^2 dk_\rho = \frac{\rho(z+z')e^{-jk_o R_i}}{R_i^5} [3 + 3jk_o R_i - k_o^2 R_i^2]. \quad (12)$$

Following the recipe given above, the five Sommerfeld integrals of interest have been approximated with an error of less than 1% in this study. In a particular propagation medium, each set of complex images is only valid in a particular spatial and spectral domain—in other words, each set affords accurate estimation only over a limited range of ρ , $(z+z')$, and frequency. (Formally, unlike that of equation 11, the right side of equation 12 is not in the proper form to be labeled as a “complex image” contribution; nonetheless, the name “method of discrete images” is adopted here when referring to this technique.)

In examining equations 5 and 6, it can be seen that for a structure supporting purely horizontal currents (e.g., distributed filter), only two Sommerfeld integrals are needed in setting up the matrix equation. Furthermore, for a general three-dimensional (3-D) structure, it has been observed that the non-diagonal components (i.e., the directionally mixed response terms G_{xz}^A , G_{zx}^A , G_{yz}^A , and G_{zy}^A) of the dyadic Green’s function have only minor contributions to the total impedance matrix.

2.2 Wideband Lumped-element Equivalent Circuit Synthesis

RF components such as transmission lines, antennas, and distributed filters are translated into equivalent circuits for subsequent simulation in a SPICE solver. The multi-port S -parameters of the structures are first obtained with the MoM technique and then transformed into Y -parameters. The frequency-domain transfer function—that is, in this case, the function representing the admittance parameter, $Y_{EM}(s)$ —for each component can be expanded as a rational approximation of the form

$$Y_{EM}(s) \approx \sum_i \frac{r_i}{s - p_i} + d + se, \quad (13)$$

where $s = j\omega$ is the complex frequency; r_i and p_i are the residues and poles, respectively; and d, e are constants. Note that r_i and p_i appear as either pure real numbers or complex conjugate pairs. After the unknown parameters in equation 13 are estimated with the two-stage vector fitting approach outlined by Gustavsen (38–41), a wideband equivalent circuit network for the RF component is synthesized by converting each term within equation 13 into a lumped-element circuit using the procedure prescribed in reference 42.

2.3 Circuit Simulation

The response of the overall equivalent network for the RF structure—consisting of the wideband lumped-element sub-circuits derived in section 2.2 and the extracted nonlinear components—is simulated in a SPICE solver. Specifically, a time-domain transient analysis is carried out to obtain the output harmonic amplitudes for an excitation at a given fundamental frequency. (Note that a harmonic-balance-based circuit simulator can also be used to realize a frequency-domain characterization [43].) A first-order approximation is employed to deduce the effective stimulus needed for the network. The re-radiated power at each harmonic can be found by evaluating the power dissipated by the radiation resistances within the equivalent circuit. The harmonic current densities on the structure, which are needed for the field pattern calculations, are approximated by the linear MoM solver (after properly terminating the structure ports with equivalent impedances).

2.4 Electromagnetic Field Propagator

Once the current distributions have been obtained with the MPIE-MoM, the radiation properties of the RF structure can be characterized by applying a propagation model in accordance with the geometry and physical properties of the propagation medium. For a current source located over a flat ground surface, a second-order asymptotic approximation can be derived from an exact solution in computing the radiated fields; the formulations necessary for this step can be deduced from the expressions given in appendix A specialized to a half-space medium. It should be mentioned that although the hybrid MoM and asymptotic propagator approach as outlined above has been described only for currents located above the air/ground interface, an equally valid and conceptually similar set of formulations and procedures exists for the subsurface case. The only major deviation results from the fact that when the radiators are submerged in a lossy medium, the mode of propagation taken by the fields may be in the form of lateral waves instead of geometric-optics contributions and Norton waves (44, 45); hence, the asymptotic propagator should be modified accordingly.

For through-wall environments, the radiation from sources located inside a room is calculated with a physical-optics and volumetric polarization current-based approach by following these steps:

1. The incident waves at the inner wall surfaces are determined by the half-space asymptotic method discussed above.
2. The incident waves—approximated as plane waves—are decomposed into transverse electric (TE) and transverse magnetic (TM) modes. By treating the walls as standard two-layer dielectric structures, the modal fields inside the walls are then estimated with the plane-wave transmission coefficients of the media.
3. The polarization currents for replacing the walls are derived from the volumetric equivalence principle as

$$\vec{J}_p(\vec{r}) = -i\omega\epsilon_o(\epsilon_r - 1)\vec{E}_w(\vec{r}); \quad (14)$$

where $\vec{E}_w(\vec{r})$ is the electric field inside the wall and ϵ_r is the complex relative dielectric constant of the wall material.

4. Subsequently, by using the half-space asymptotic propagator, the signal outside the room is found by summing the radiation from the wall polarization currents and the direct radiation due to the RF structure in the absence of the room:

$$\vec{E}_{total}(\vec{r}) \propto \int_{wall} \vec{\bar{G}}_{hs}(\vec{r}, \vec{r}') \cdot \vec{J}_p(\vec{r}') d\vec{r}' + \int_{RF\ structure} \vec{\bar{G}}_{hs}(\vec{r}, \vec{r}') \cdot \vec{J}_s(\vec{r}') d\vec{r}', \quad (15)$$

where $\vec{\bar{G}}_{hs}(\vec{r}, \vec{r}')$ is the half-space dyadic Green's function from appendix A.

The advantages of the outlined semi-analytic approach are that it is computationally faster and more efficient than an exact full-wave method, and it has the ability to incorporate surface-wave contributions into the solution. The shortcoming is that the technique only provides an approximate solution: only the first-order wall reflection/scattering effects are included in the solution. (Note that multiple reflections *within* the walls are taken into account for the calculation of the fields in step 2.) To improve the accuracy of the solver, an iterative physical-optics routine can be used to include shadowing and higher-order effects.

3. Numerical Examples: Applications of the Hybrid Solver

3.1 Circuit-Component-Loaded Scatterer in Half-space Environment

As most RF transceivers contain an antenna and a filter element at their front-ends, the structure in figure 4 is chosen for illustrative purposes in this section. The filter is a microstrip dual-band bandpass filter with operational bands at ~900 MHz and ~2000 MHz. The dual-band topology results from the use of the combination of a broadband shunt stub bandpass filter and an open-stub bandstop filter. The broadband bandpass and bandstop filters basically composed of *approximately* quarter-wavelength long stubs spaced by quarter-wavelength transmission line

sections. Separately, the two filters can be translated into transmission line-based structures by applying Richard's transformation to their respective lumped-element-based, low-pass/bandpass/bandstop prototypes. The antenna—connected to the microstrip filter and printed on the other side of the two-layer substrate—is a dual-band, slot-loaded microstrip circular patch, with the feeding point at an off-center position. A shorting connection is added at the center to reduce the size of the patch. Essentially, the patch behaves as a quarter-wave radiator, and the fundamental mode of the circular cavity provides the resonance at the lower frequency band, whereas the slot supplies the resonance at the higher frequency band. (Note that dual-band performance for the center-shortened circular cavity can also be established without the slot. However, it is seen in the initial design that the second resonance frequency of the cavity is higher than predicted. The presence of the slot enables the generation of the needed response at ~1900–2000 MHz while maintaining a compact geometry. Consequently, the second resonance of the cavity is affected by the slot, but the first resonance is not.) To introduce a nonlinear element into the structure, a varactor is added to the antenna, providing capacitive tuning capability. The effective capacitance of the varactor as a function of the DC bias voltage is shown in figure 5. Simulations of the filter and the antenna are carried out using the linear MoM approach from section 2—assuming infinite, layered substrates. The S -parameters of the components are shown in figures 6 and 7.

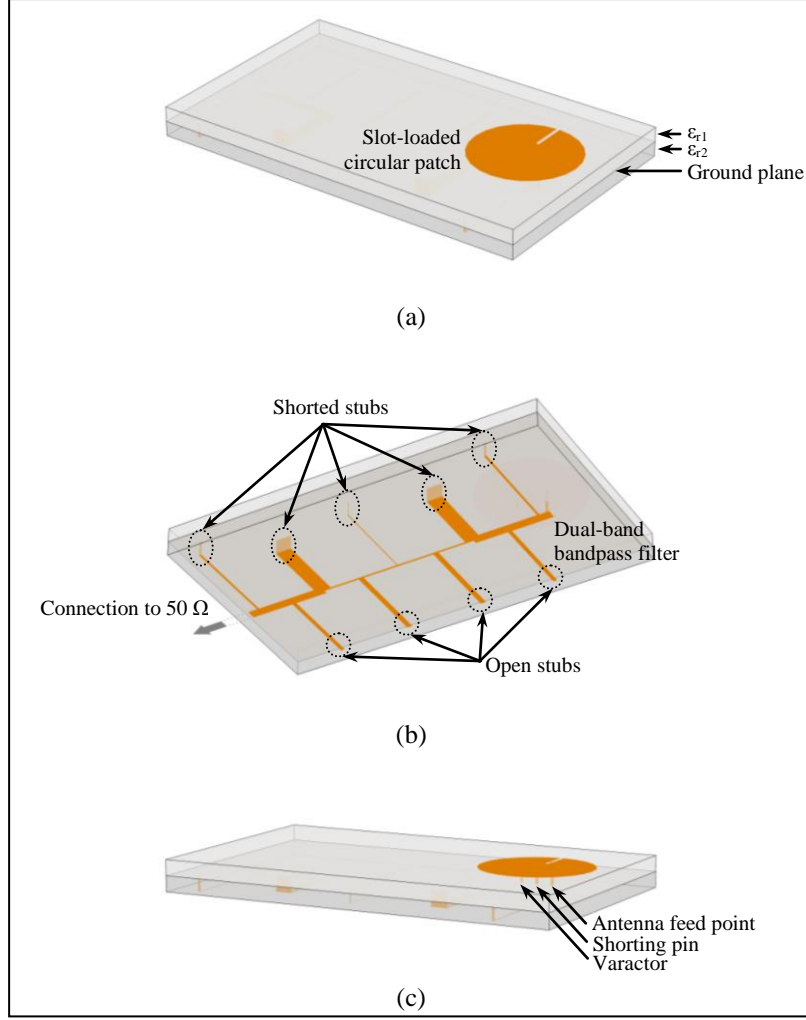


Figure 4. Antenna and filter for RF front-end: (a) top view; (b) bottom view; and (c) side view. $\epsilon_{r1} = \epsilon_{r2} = 4.5$ ($\tan\delta \approx 0.04$); the thickness of each substrate is 1.6 mm. The distributed filter has dimensions $\sim 10.7 \text{ cm} \times 7 \text{ cm}$; the radius of the circular patch antenna is 1.79 cm, and the length of the slot is 1.14 cm.

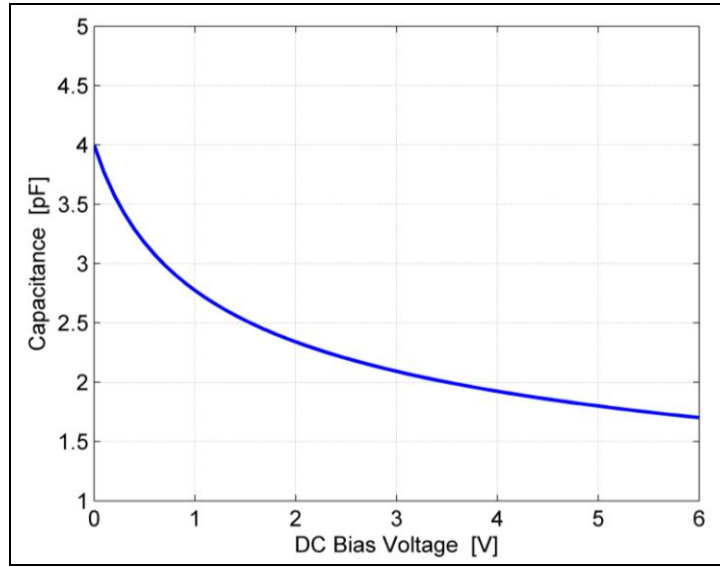


Figure 5. Effective capacitance of varactor used in the setup shown in figure 4 as function of DC bias voltage.

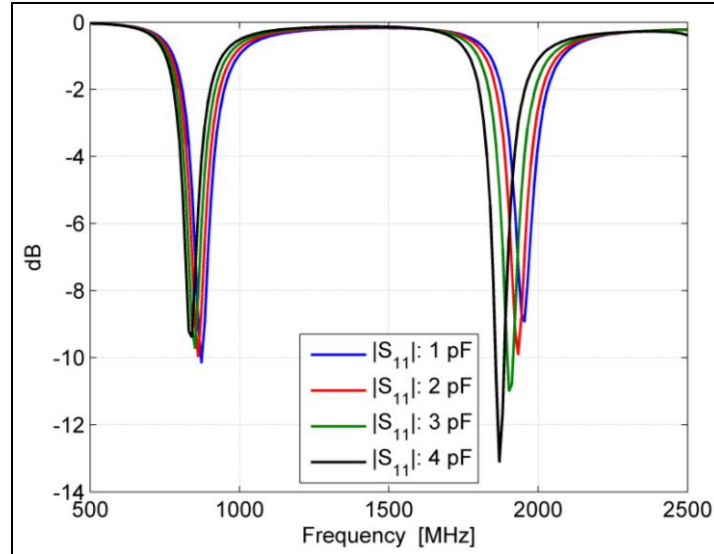


Figure 6. $|S_{11}|$ for the dual-band, slot-loaded circular patch antenna as function of frequency and varactor capacitance.

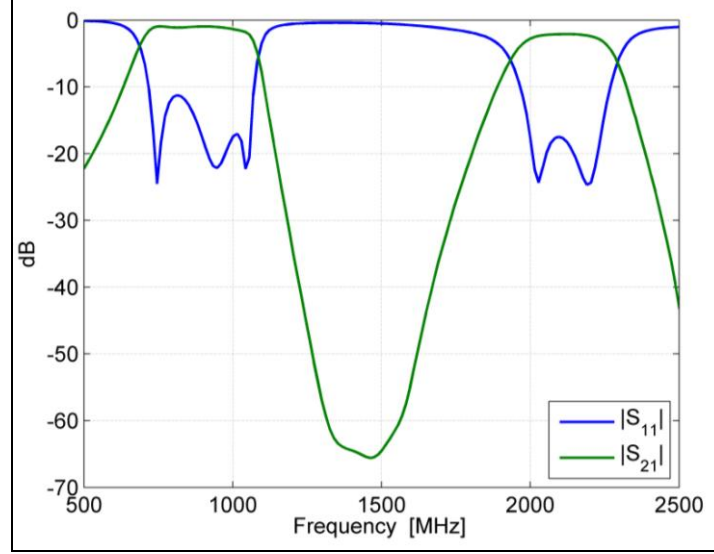


Figure 7. S -parameters for microstrip dual-band bandpass filter as function of frequency.

The scattering from the RF structure in figure 4 is calculated with the hybrid approach put forth in section 2. Note that for the analysis that follows, it is assumed that the filter input has been terminated with a $50\ \Omega$ load and the varactor is biased at 0 V. The structure is placed at 10 cm below the ground surface (the ground has relative dielectric constant $\epsilon_r' = 4$ and conductivity $\sigma_d = 10\ \text{mS/m}$). The excitation is provided by a vertical electric dipole—located 10 m from the scatterer at a 2-m height—transmitting a monochromatic wave with $f_o = 840\ \text{MHz}$. Figure 8 shows the backscattered responses of the scatterer at the fundamental and the second harmonic for two levels of transmitted power—that is, for $P_{TX} = 100\ \text{W}$ and $1000\ \text{W}$. The received power at the receiver is estimated by first propagating the fields from the scatterer using the asymptotic solver and then calculating the power intercepted by a polarization-matched receiving antenna with 0 dB gain. The near-quadratic dependence of the scattered power at $2f_o$ on the transmitted power is evident. The instability of the time-domain SPICE solver prevents the responses at the higher-order harmonics to be derived here; however, note that an accurate spectrum characterization may be found using a harmonic-balance-based circuit simulator. Figure 9 shows the variation of the scattered fields as a function of the azimuth angle.

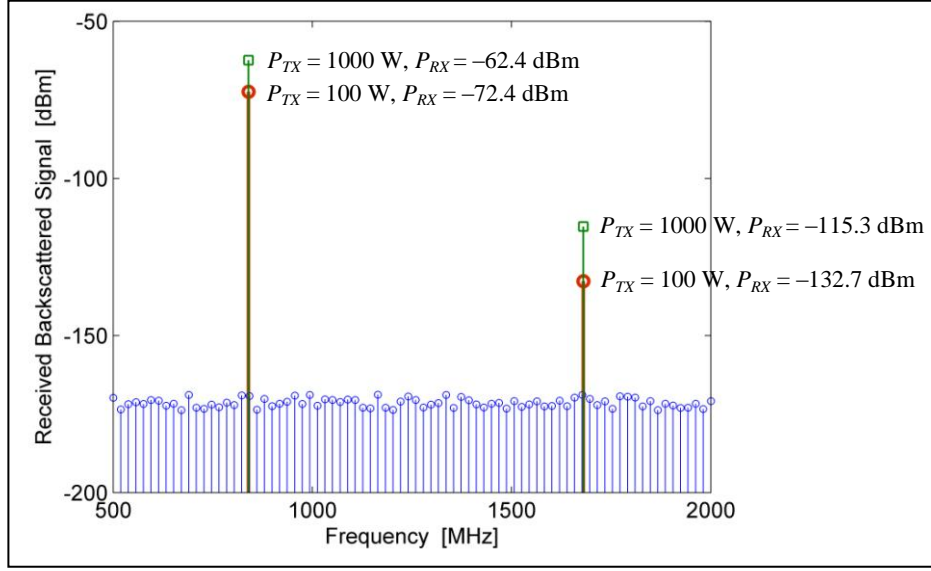


Figure 8. Backscattered response of scatterer in figure 4 at fundamental and second harmonic for two levels of transmitted power. The noise floor (kT) shown is at -173.8 dBm/Hz.

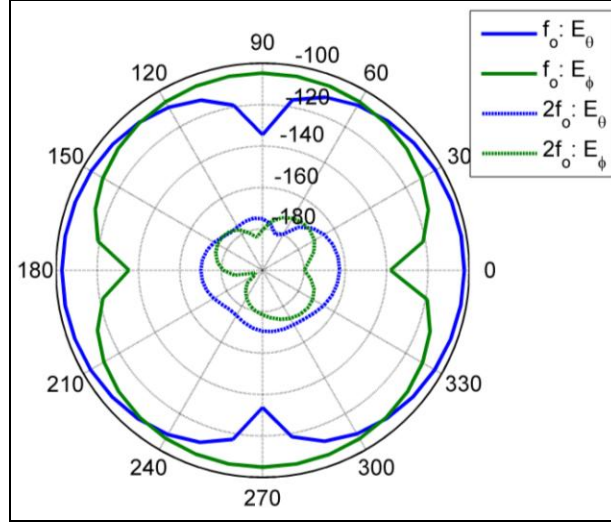


Figure 9. Variation of scattered electric field components as a function of azimuth angle.

To investigate the decay of the signal as a function of sensing distance, the backscattered responses are calculated for three different standoff ranges— $r = 10$ m, 30 m, and 100 m. The results in figure 10 demonstrate that the fundamental scattering component falls off as $\propto r^{-8}$, whereas the second harmonic falls off as $\propto r^{-12}$. These behaviors are consistent with theoretical results derived using analytical models for the nonlinear circuit response and field propagation. As a generalization, in the asymptotic regime, it can be shown that—for the backscattering-based sensing scenario in which the interaction points are positioned close to the ground surface—the n -th harmonic return approximately depends on the distance as $\propto r^{-4(n+1)}$.

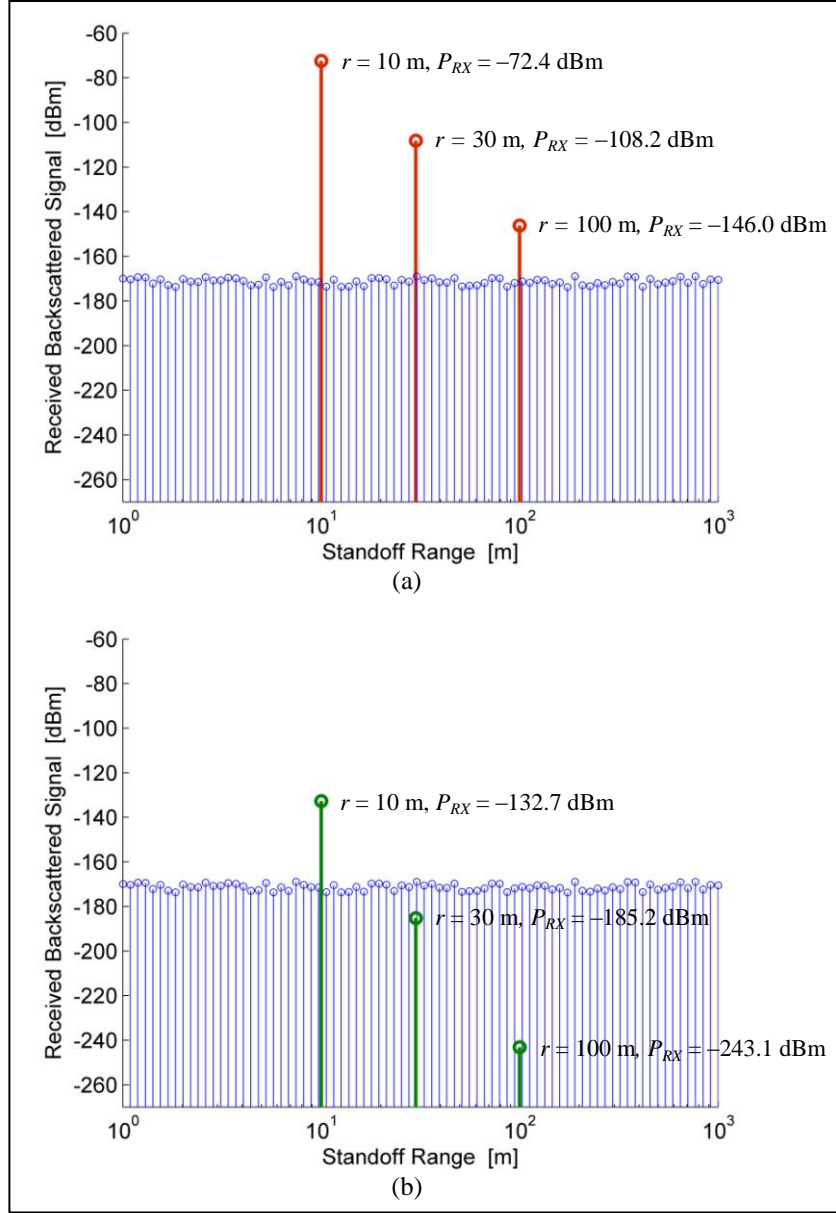


Figure 10. Backscattered response as a function of range: (a) f_o and (b) $2f_o$.

To see the effects of a more complicated nonlinear load on the scattering response, a low-noise, traveling-wave amplifier is connected at the filter input port. The design and circuit layout for the amplifier are considered in detail within appendix C; a two-stage topology (figure C-6a) is employed for the scattering analysis here. The received power level as a function of frequency—up to the third harmonic—is displayed in figure 11 for the monochromatic incidence case; the simulation parameters are the same as those of figure 8. It should be mentioned that, for this example problem, in addition to the amplifier, more components—passive and active, linear and nonlinear—can be connected to the RF structure. These components are “transparent” to the electromagnetic solver—that is, they are replaced only by equivalent loads in the field analysis,

for calculating the effective system stimulus and the structure current densities; full circuit models of these components, however, can be included in the SPICE solver to characterize the circuit spectral response.

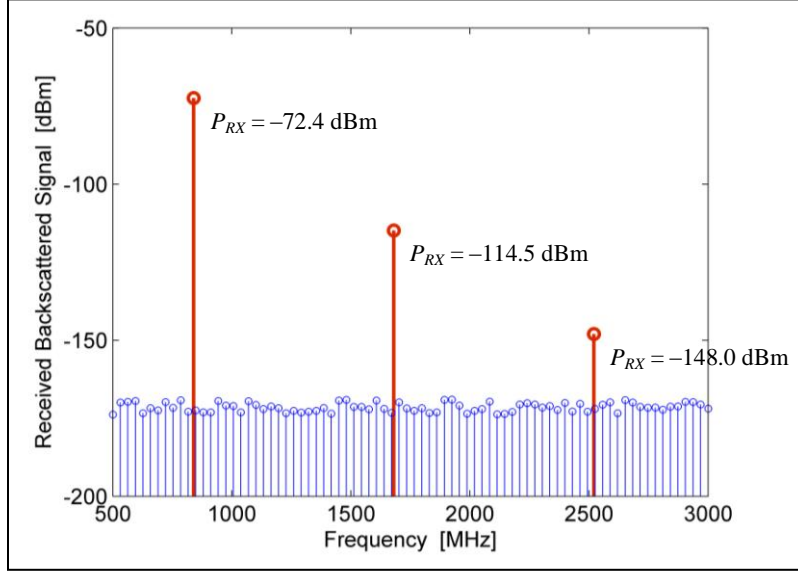


Figure 11. Backscattered responses at fundamental, second, and third harmonics of scatterer in figure 4 connected to a traveling-wave amplifier.

Once the scattered fields from the RF structure are obtained, an imaging algorithm can be used to process the return signals for localization. In this work, a time-reversal-based MUSIC (TR-MUSIC) algorithm is applied to generate the imaging functional. Consider the multi-static sensing of a scene with M nonlinear scatterers using an N -element array, the scattered field response (at frequency ω_s) received at the array due to excitation (at frequency ω_i) by the n -th transmitter of the array can be shown to be

$$\begin{aligned} \vec{S}_m(\omega_s, \omega_i) = & \sigma_{s1}(\omega_s, \omega_i) G(\vec{r}_{s1}, \vec{r}_n, \omega_i) \begin{bmatrix} G(\vec{r}_1, \vec{r}_{s1}, \omega_s) \\ G(\vec{r}_2, \vec{r}_{s1}, \omega_s) \\ \vdots \\ G(\vec{r}_N, \vec{r}_{s1}, \omega_s) \end{bmatrix} + \sigma_{s2}(\omega_s, \omega_i) G(\vec{r}_{s2}, \vec{r}_n, \omega_i) \begin{bmatrix} G(\vec{r}_1, \vec{r}_{s2}, \omega_s) \\ G(\vec{r}_2, \vec{r}_{s2}, \omega_s) \\ \vdots \\ G(\vec{r}_N, \vec{r}_{s2}, \omega_s) \end{bmatrix} + \cdots + \sigma_{sM}(\omega_s, \omega_i) G(\vec{r}_{sM}, \vec{r}_n, \omega_i) \begin{bmatrix} G(\vec{r}_1, \vec{r}_{sM}, \omega_s) \\ G(\vec{r}_2, \vec{r}_{sM}, \omega_s) \\ \vdots \\ G(\vec{r}_N, \vec{r}_{sM}, \omega_s) \end{bmatrix} \quad (16) \\ = & \sigma_{s1}(\omega_s, \omega_i) G(\vec{r}_{s1}, \vec{r}_n, \omega_i) \vec{G}(\vec{r}_{s1}, \omega_s) + \sigma_{s2}(\omega_s, \omega_i) G(\vec{r}_{s2}, \vec{r}_n, \omega_i) \vec{G}(\vec{r}_{s2}, \omega_s) + \cdots + \sigma_{sM}(\omega_s, \omega_i) G(\vec{r}_{sM}, \vec{r}_n, \omega_i) \vec{G}(\vec{r}_{sM}, \omega_s); \end{aligned}$$

where \vec{r}_n ($n = 1, 2, \dots, N$) is the location of the n -th array element, \vec{r}_{sm} ($m = 1, 2, \dots, M$) is the location of the m -th scatterer, $\sigma_{sm}(\omega_s, \omega_i)$ is the scattering strength of the m -th scatterer, and $G(\vec{r}, \vec{r}', \omega)$ is the Green's function of the environment. From equation 16, it is seen that the scattered field signal subspace is spanned by the Green's function vectors $\vec{G}(\vec{r}_{s1}, \omega_s)$, $\vec{G}(\vec{r}_{s2}, \omega_s)$, \dots , $\vec{G}(\vec{r}_{sM}, \omega_s)$ —in other words, the scatterer locations are encoded within the subspace representation of the received signal (46). In more concise form, after invoking the reciprocity

principle, the frequency-domain $N \times N$ multi-static scattered signal matrix for the array can be written as

$$\mathbf{K}(\omega_s, \omega_i) = \sum_{m=1}^M \sigma_{sm}(\omega_s, \omega_i) \vec{G}(\vec{r}_{sm}, \omega_s) \vec{G}^T(\vec{r}_{sm}, \omega_i), \quad (17)$$

in which T represents the transpose operation, and the matrix element $K_{pq}(\omega_s, \omega_i)$ is the response at the p -th array element due to excitation at the q -th array element. In practical applications, $\mathbf{K}(\omega_s, \omega_i)$ is simply taken as the measurement matrix. For image generation, the signal subspace of $\mathbf{K}(\omega_s, \omega_i)$ is computed using a singular value decomposition procedure:

$$\mathbf{K}(\omega_s, \omega_i) = \mathbf{U}(\omega_s, \omega_i) \mathbf{\Lambda}(\omega_s, \omega_i) \mathbf{V}(\omega_s, \omega_i)^H, \quad (18)$$

where $\mathbf{U}(\omega_s, \omega_i)$ and $\mathbf{V}(\omega_s, \omega_i)$ are unitary matrices, $\mathbf{\Lambda}(\omega_s, \omega_i)$ contains the singular values of $\mathbf{K}(\omega_s, \omega_i)$, and H denotes the conjugate transpose operation. Noting that the column vectors of $\mathbf{U}(\omega_s, \omega_i)$ supply the eigenvectors $\hat{u}_p(\omega_s, \omega_i)$ ($p = 1, 2, \dots, N$), and assuming that the scattered signal subspace is spanned by the eigenvectors corresponding to the first L significant (or non-zero) eigenvalues and the null subspace is spanned by the remaining eigenvectors corresponding to the non-significant (or zero) eigenvalues, an imaging functional can be constructed as

$$O(\vec{r}, \omega_s, \omega_i) = \left(\sum_{p=L+1}^N \left| \langle \hat{u}_p(\omega_s, \omega_i), \vec{G}(\vec{r}, \omega_s) \rangle \right|^2 \right)^{-1}, \quad (19)$$

where the Green's function vector $\vec{G}(\vec{r}, \omega_s)$ can be computed using numerical or analytical methods. The imaging functional in equation 19 peaks at the scatterer locations. In effect, then, an image of the scene can be derived using the scattering response at a *single* receiving frequency. To increase the stability of the algorithm, equation 19 can be performed over multiple receiving frequencies (e.g., harmonics) or a band of receiving frequencies:

$$O(\vec{r}, \Omega, \omega_i) = \left(\sum_{\Omega} \sum_{p=L(\omega_s, \omega_i)+1}^N \left| \langle \hat{u}_p(\omega_s, \omega_i), \vec{G}(\vec{r}, \omega_s) \rangle \right|^2 \right)^{-1}, \quad \omega_s \in \Omega, \quad (20)$$

in which Ω denotes the range of available receiving frequencies. Equations 19 and 20 can also be generalized to accommodate scenarios in which multiple excitation frequencies (multi- ω_i) are utilized. (Note that TR-MUSIC based on the conventional, or linear, scattering response is derived by setting $\omega_s = \omega_i$ in equations 16–20.)

The imaging functional in equation 19 is employed for imaging the scenario displayed in figure 12. The scene consists of the circuit-component-loaded scatterer from figure 4 buried in the ground, along with two (linear) clutter objects. The sensing array is composed of $N = 16$ transceivers distributed over a 2-m wide aperture and the standoff range is ~ 6.6 m. The harmonic multi-static scattered signal matrices of the scene at f_o and $2f_o$ are calculated with the hybrid

solver. $\vec{G}(\vec{r}, \omega_s)$ in equation 19 is calculated with the formulations in appendix A (or reference 24). The images at the two frequencies are included in figure 12. Note that the target is accurately localized in both images, but the clutter signal components do not show up in the image at $2f_o$.

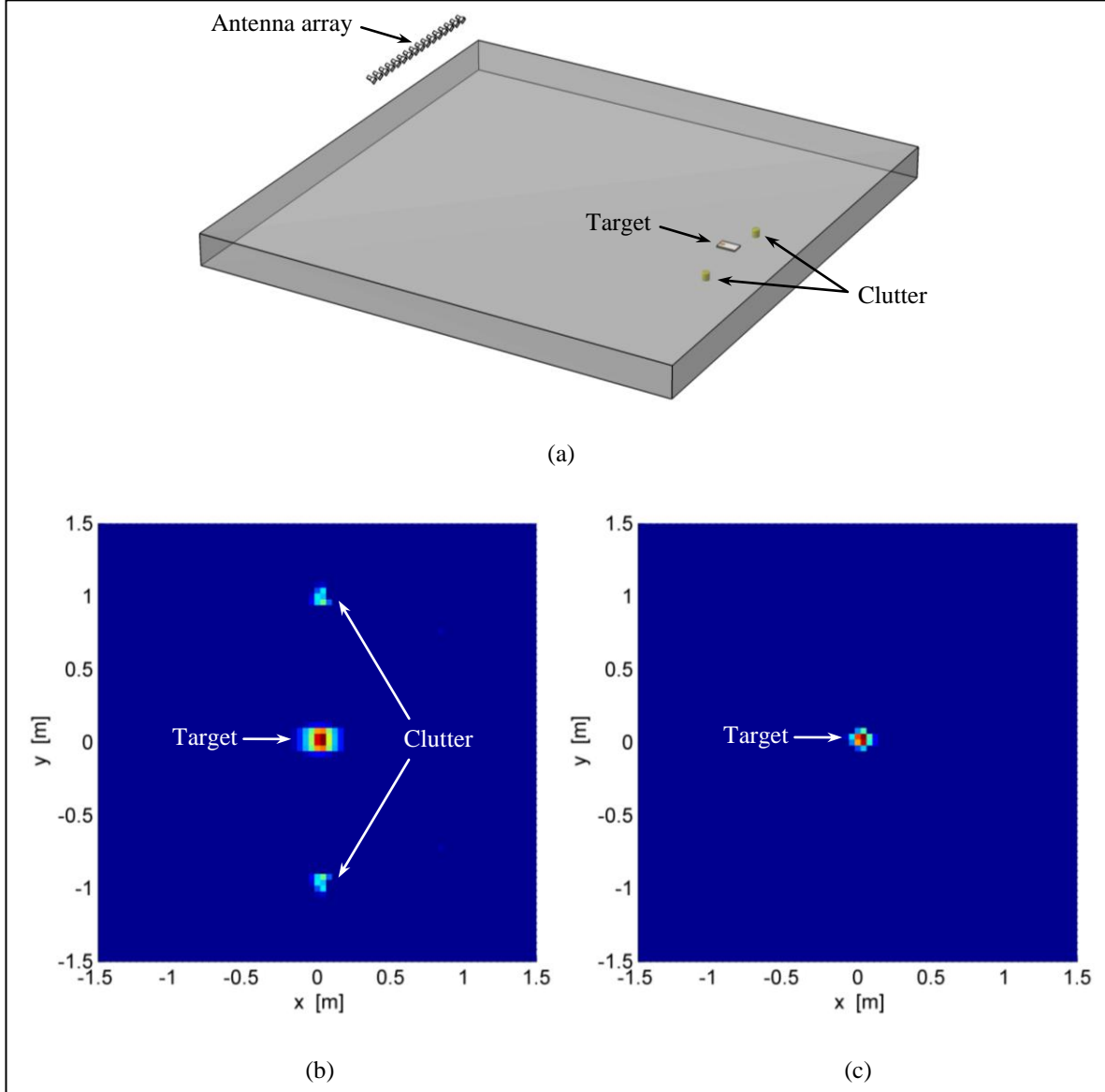


Figure 12. Imaging results for a buried target scenario: (a) Scene containing target and clutter, (b) image generated using scattering response at $f_o = 840$ MHz (both the target and clutter are imaged), and (c) image generated using scattering response at $2f_o = 1680$ MHz (only the target is captured).

3.2 Circuit-Component-Loaded Scatterer in Room Environment

To investigate the response of a circuit-component-loaded scatterer for through-wall sensing applications, the RF structure from section 3.1 is placed in the room environment shown in

figure 2. In this example, the walls, ground, and roof (not shown in figure 2) are homogenous media with $\epsilon_r' = 6$ and $\sigma_d = 30$ mS/m. Note that as before, the filter input has been terminated with a $50\ \Omega$ load and the varactor is biased at 0 V. The RF structure is placed at 1 m above the ground; the excitation is provided by a vertical electric dipole located outside the room at a height of 1 m, transmitting at $f_o = 840$ MHz, with $P_{TX} = 100$ W; and a receiving antenna (co-located with the transmitter) with 0 dB gain is assumed. The hybrid solver outlined in section 2 is applied for deriving the backscattered responses at f_o and $2f_o$. To calculate the initial incident field on the RF structure, the reciprocity principle is exploited: the locations of the transmitter and observation point are interchanged and then the fields are propagated with the physical-optics and volumetric polarization current-based approach from section 2.4. Figure 13 shows the backscattered responses of the scatterer at the fundamental and the second harmonic. The bistatic scattering pattern as a function of azimuth angle is shown in figure 14.

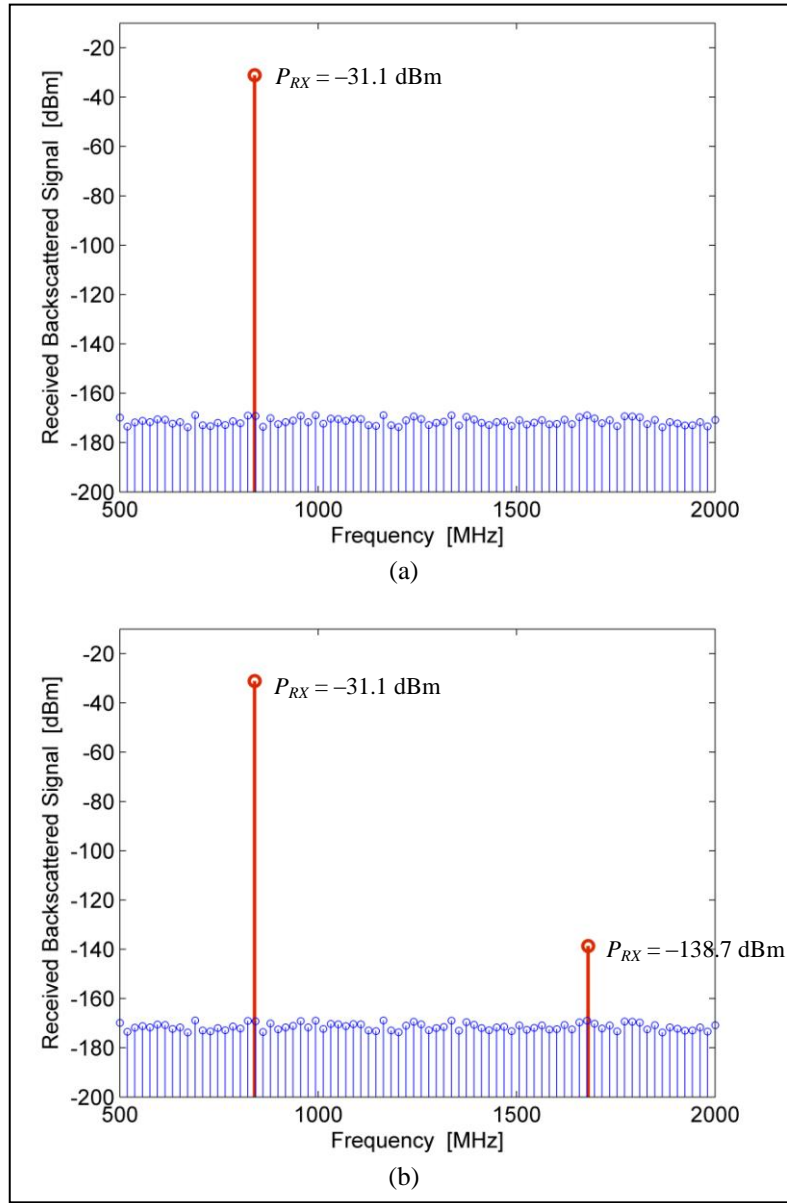


Figure 13. Backscattered response of scenario shown in figure 2: (a) without and (b) with circuit-component-loaded scatterer in room.

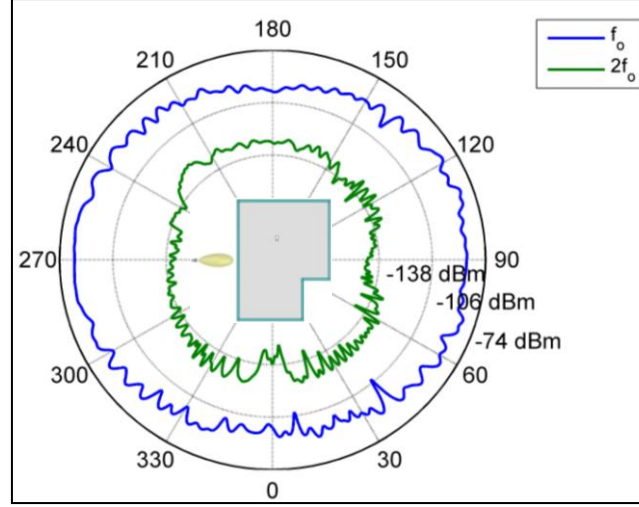


Figure 14. Backscattered response at fundamental and second harmonic as function of azimuth angle for scenario in figure 2.

In order to verify the accuracy of the field propagator in the presence of a wall, simulation results are compared with measurement data obtained by Dagefu and Sarabandi (47). The wall is solid concrete with $\epsilon_r' = 4$ and $\sigma_d = 20$ mS/m and has dimensions $2.56 \text{ m} \times 1.56 \text{ m} \times 0.09 \text{ m}$. Two setups are considered. In the first case (figure 15a), the transmitter is located 1.74 m from the wall at a height of 0.87 m; the signal strength along an observation line 0.91 m from the wall at 0.79 m height is recorded. In the second case (figure 16a), the transmitter is located 1.74 m from the wall at a height of 0.24 m; the signal strength along an observation line perpendicular to the wall at 0.20 m height is recorded. In this example, for the electromagnetic simulations, $f_o = 2$ GHz. Note that the measurement scenario only considers the linear propagation effects at the fundamental frequency of interest. Figures 15b and 16b show that there is good agreement between the analytically derived results and the measured data.

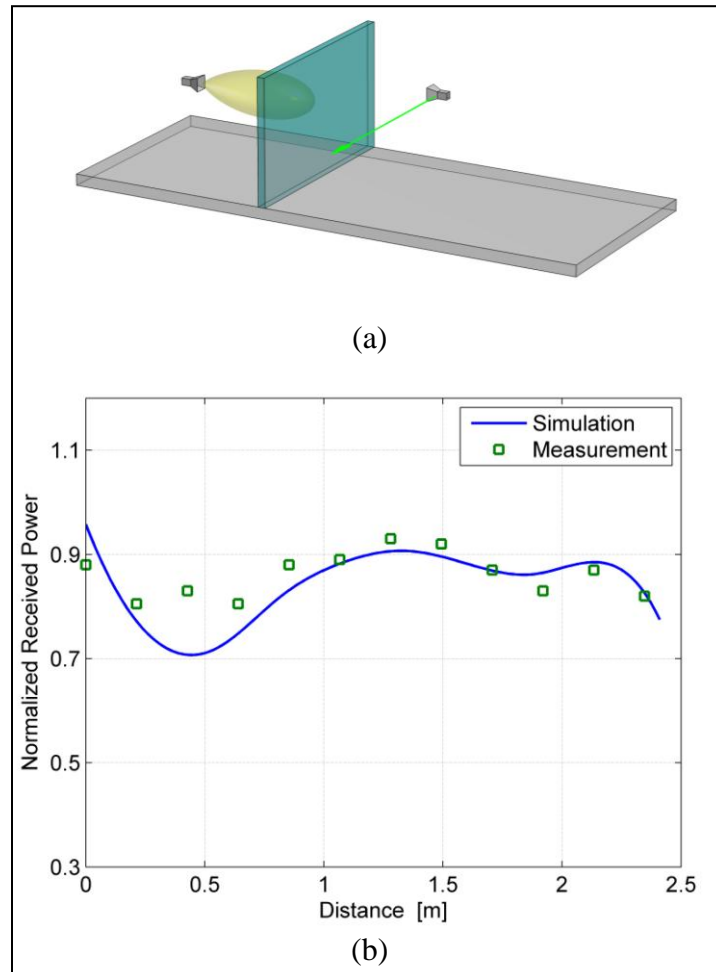


Figure 15. Simulated vs. measured responses for propagation in presence of a wall.

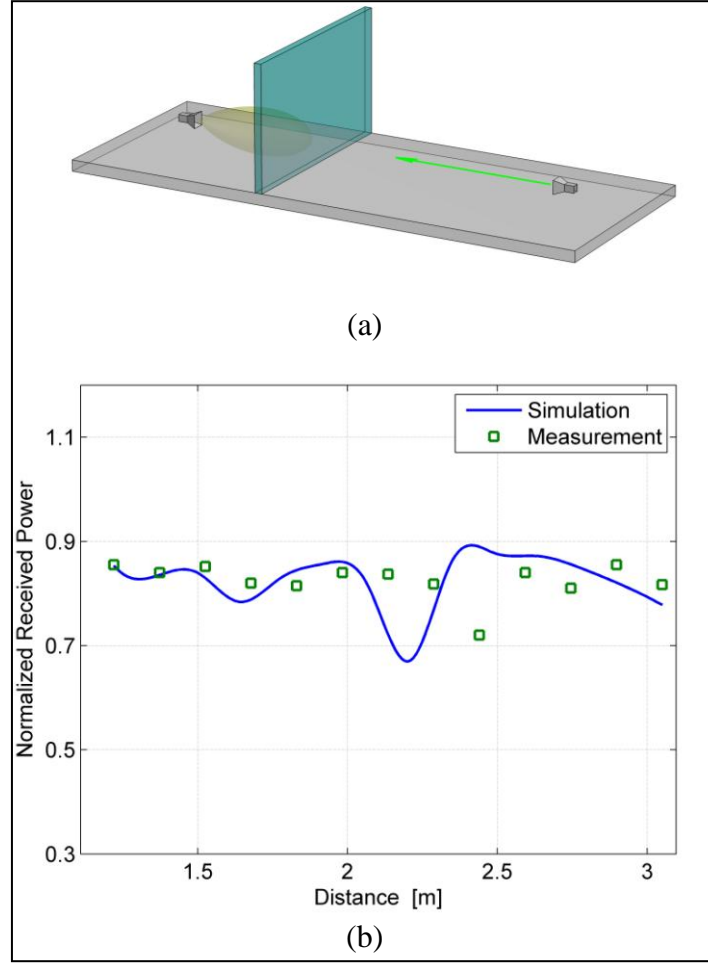


Figure 16. Simulated vs. measured responses for propagation in presence of a wall.

4. Conclusions

To study the radio harmonic scattering responses of circuit-component-loaded objects, a hybrid electromagnetic/circuit solver is developed in this work. The proposed numerical analysis approach exploits a combination of 3-D electromagnetic simulations (based on full-wave and asymptotic techniques) in the propagation and RF component domains and SPICE simulations in the circuit domain. In sum, a systematic strategy—one which is capable of tracking the signal interactions from the transmitter terminal to the receiver terminal—is established for attaining generalized solutions of the multiscale harmonic scattering problem. This *terminal-to-terminal* (or *end-to-end*) solver has been applied to two common radar sensing problems of interest. In particular, considered herein in detail are the linear and nonlinear scattering effects from an RF circuit-loaded object placed in either near-ground or through-wall settings. The scattering responses as functions of excitation power, sensing range, and azimuth angle are examined, and

the localization, or imaging, of the scatterer using both the linear and the nonlinear returns has also been investigated. Through the theoretical developments and illustrative examples put forth, it is demonstrated that the proposed hybrid solver—though not completely full-wave-based—establishes a practical and computationally efficient solution process for characterizing harmonic scattering in complex environments.

5. References

1. Picket-May, M.; Taflove, A.; Baron, J. FD-TD Modeling of Digital Signal Propagation in 3-D Circuits With Passive and Active Loads. *IEEE Trans. Microw. Theory and Techniques* **Aug. 1994**, 43 (8), 1514–1523.
2. Sui, W.; Christensen, D. A.; Durney, C. H. Extending the Two-Dimensional FD-TD Method to Hybrid Electromagnetic Systems With Active and Passive Lumped Elements. *IEEE Trans. Microw. Theory and Techniques* **Apr. 1992**, 40, 726–730.
3. Ciampolini, P.; Mezzanotte, P.; Roselli, L.; Sorrentino, R. Accurate and Efficient Circuit Simulation With Lumped-Element FDTD Technique. *IEEE Trans. Microw. Theory and Techniques* **Dec. 1996**, 44 (12), 2207–2215.
4. Pereda, J. A.; Alimenti, F.; Mezzanotte, P.; Roselli, L.; Sorrentino, R. A New Algorithm for the Incorporation of Arbitrary Linear Lumped Networks into FDTD Simulators. *IEEE Trans. Microw. Theory and Techniques* **Jun. 1999**, 47 (6), 943–949.
5. Huang, C.-C.; Chu, T.-H. Analysis of Wire Scatterers with Nonlinear or Time-Harmonic Loads in the Frequency Domain. *IEEE Trans. Antennas and Propagation* **Jan. 1993**, 41 (1), 25–30.
6. Parron, J.; Collado, C.; Mateu, J.; Rius, J. M.; Duffo, N.; O'Callaghan, J. M. General Electromagnetic Simulation Tool to Predict the Microwave Nonlinear Response of Planar, Arbitrarily-Shaped HTS Structures. *IEEE Trans. Applied Superconductivity* **Mar. 2001**, 11 (1), 399–402.
7. Liu, T. K.; Tesche, F. M. Analysis of Antennas and Scatterers with Nonlinear Loads. *IEEE Trans. Antennas and Propagation* **Mar. 1976**, 24, 131–139.
8. Liu, T. K.; Tesche, F. M.; Deadrick, F. J. Transient Excitation of an Antenna with a Nonlinear Load: Numerical and Experimental Results. *IEEE Trans. Antennas and Propagation* **Jul. 1977**, 25, 539–542.
9. Sarkar, T. K.; Weiner, D. D. Scattering Analysis of Nonlinearly Loaded Antennas. *IEEE Trans. Antennas and Propagation* **Mar. 1976**, 24, 125–131.
10. Zaboronkova, T. M.; Gorbachev, A. A.; Vasenkov, A. A. Nonlinear Electromagnetic Wave Scattering by Loaded Dipole Antennas. *Applied Electromagnetism, Proc. Second International Symposium of Trans. Black Sea Region*, pp. 5–6, 2000.
11. Kanda, M. Analytical and Numerical Techniques for Analyzing an Electrically Short Dipole With a Nonlinear Load. *IEEE Trans. Antennas and Propagation* **Jan. 1980**, 28, 71–78.

12. Luebbers, R.; Beggs, J.; Chamberlin, K. Finite Difference Time-Domain Calculation of Transients in Antennas with Nonlinear Loads. *IEEE Trans. Antennas and Propagation* **May 1993**, *41* (5), 566–573.
13. Porti, J. A.; Morente, J. A. A Numerical Analysis of Wire Antennas Loaded With Varistor-Composite Materials. *IEEE Trans. Electromagn. Compat.* **Feb. 1994**, *36* (1), 23–31.
14. Lee, K. C. An Efficient Algorithm for the Steady-State Analysis of a Nonlinearly Loaded Antenna Array. *J. Electromagn. Waves Applicat.* **2000**, *14*, 1373–1382.
15. Analysis of Large Nonlinearly Loaded Antenna Arrays under Multitones Excitation,” *Microw. Opt. Technol. Lett.* **Jun. 2000**, 319–323.
16. Two Efficient Algorithms for the Analyses of a Nonlinearly Loaded Antenna and Antenna Array in the Frequency Domain. *IEEE Trans. Electromagn. Compat.* **Nov. 2000**, *45* (4), 339–346.
17. Genetic Algorithms Based Analyses of Nonlinearly Loaded Antenna Arrays Including Mutual Coupling Effects,” *IEEE Trans. Antennas and Propagation* **Apr. 2003**, *51* (4), 776–781,.
18. Kalialakis, C.; Hall, P. S. Analysis and Experiment on Harmonic Radiation and Frequency Tuning of Varactor-Loaded Microstrip Antennas. *IET Microw. Antennas Propagation* **Apr. 2007**, *1* (2), 527–535.
19. Zheng, Y.; Hristov, A.; Giere, A.; Scheele, P.; Jakoby, R. Analysis on Harmonic Radiation of Capacitively Loaded Tunable PIFA Based on Equivalent Circuit. *Frequenz*, **2007**, *61*, 213–216.
20. Cui, J.; Zhang, M. Transient Analysis of PCB EMC Problem. *8th International Symposium on Antennas Propagation and EM Theory, ISAPE 2008*, pp. 1111–1114, Nov. 2008.
21. Kung, F.; Chuah, H.-T. A Finite-Difference Time-Domain (FDTD) Software for Simulation of Printed Circuit Board (PCB) Assembly. *Progress In Electromagnetics Research* **2005**, *50*, 299–335.
22. Çakir, G.; Çakir, M.; Sevgi, L. Electromagnetic Radiation from Multilayer Printed Circuit Boards: A 3D FDTD-Based Virtual Emission Predictor. *Turk J Elec Eng and Comp Sci* **2009**, *17* (3), 315–325.
23. Asai, H.; Watanabe, T.; Sasaki, T.; Araki, K. An EMI Simulator Based on the Parallel-Distributed FDTD Method for Large-Scale Printed Wiring Boards. *Proc. 6th IEEE Workshop on Signal Propagation on Interconnects*, pp. 141–144, May 2002.
24. Liao, D. H. *Physics-Based Near-Earth Radiowave Propagation Modeling and Simulation*, Ph.D. Thesis, The University of Michigan, 2009.

25. Liao, D. H.; Sarabandi, K. Terminal-to-Terminal Hybrid Full-Wave Simulation of Low-Profile, Electrically-Small, Near-Ground Antennas. *IEEE Trans. Antennas and Propagation* **Mar. 2008**, 56 (3), 806–814.
26. Michalski, K. A.; Zheng, D. Electromagnetic Scattering and Radiation by Surfaces of Arbitrary Shape in Layered Media, Part I: Theory. *IEEE Trans. Antennas and Propagation* **Mar. 1990**, 38, 335–344.
27. Electromagnetic Scattering and Radiation by Surfaces of Arbitrary Shape in Layered Media, Part II: Implementation and Results for Contiguous Half-Spaces. *IEEE Trans. Antennas and Propagation* **Mar. 1990**, 38, 345–352.
28. Michalski, K. A. On the Scalar Potential of a Point Charge Associated with a Time-Harmonic Dipole in a Layered Medium. *IEEE Trans. Antennas and Propagation* **Nov. 1987**, 35, 1299–1301.
29. Rao, S. M. Electromagnetic Scattering and Radiation of Arbitrarily-Shaped Surfaces by Triangular Patch Modeling,” Ph. D. dissertation, The University of Mississippi, Aug. 1980.
30. Rao, S. M.; Wilton, D. R.; Glisson, A. W. Electromagnetic Scattering by Surfaces of Arbitrary Shape. *IEEE Trans. Antennas and Propagation* **May 1982**, 30, 409–418.
31. Eibert, T. F.; Hansen, V. On the Calculation of Potential Integrals for Linear Source Distributions on Triangular Domains. *IEEE Trans. Antennas and Propagation* **Dec. 1995**, 43, 1499–1502.
32. Graglia, R. D. On the Numerical Integration of the Linear Shape Functions Times the 3-D Green’s Function or Its Gradient on a Plane Triangle. *IEEE Trans. Antennas and Propagation* **Oct. 1993**, 41, 1448–1455.
33. Rao, S. M.; Glisson, A. W.; Wilton, D. R.; Vidula, B. S. A Simple Numerical Solution Procedure for Statics Problems Involving Arbitrary-Shaped Surfaces. *IEEE Trans. Antennas and Propagation* **Dec. 1979**, 27, 604–608.
34. Hua, Y.; Sarkar, T. K. Generalized Pencil-of-Function Method for Extracting Poles of an EM system from Its Transient Response. *IEEE Trans. Antennas and Propagation* **Feb. 1989**, 37, 229–234.
35. Sarkar, T. K.; Pereira, O. Using the Matrix Pencil Method to Estimate the Parameters of a Sum of Complex Exponentials,” *IEEE Antennas and Propagation Magazine* **Feb. 1995**, 37, 48–55.
36. Shuley, N. V.; Boix, R. R.; Medina, F.; Horno, M. On the Fast Approximation of Green’s Functions in MPIE Formulations for Planar Layered Media. *IEEE Trans. Microw. Theory and Techniques* **Sep. 2002**, 50, 2185–2192.

37. Hellen, M. K.; Craddock, I. J. Improving the Accuracy of the Complex Image Technique. *Microw. Optical Technology Letters* **Mar. 2001**, 28, 402–406.
38. Gustavsen, B.; Semlyen, A. Rational Approximation of Frequency Domain Responses by Vector Fitting. *IEEE Trans. Power Delivery* **Jul. 1999**, 14 (3), 1052–1061.
39. Gustavsen, B. Improving the Pole Relocating Properties of Vector Fitting. *IEEE Trans. Power Delivery* **Jul. 2006**, 21 (3), 1587–1592.
40. Morched, A.; Gustavsen, B.; Tartibi, M. A Universal Model for Accurate Calculation of Electromagnetic Transients on Overhead Lines and Underground Cables. *IEEE Trans. Power Delivery* **Jul. 1999**, 14 (3), 1032–1038.
41. Gustavsen, B. Wide Band Modeling of Power Transformers. *IEEE Trans. Power Delivery* **Jan. 2004**, 19 (1), 414–422.
42. Antonini, G. SPICE Equivalent Circuits of Frequency-Domain Responses. *IEEE Trans. Electromagnetic Compatibility* **Aug. 2003**, 45 (3), 502–512.
43. Kundert, K. S.; Sangiovanni-Vincentelli, A. Simulation of Nonlinear Circuits in the Frequency Domain. *IEEE Trans. Computer-Aided Design of Integrated Circuits and Systems* **Oct. 1986**, 5 (4), 521–535.
44. Liao, D. H.; Sarabandi, K. Near-Earth Wave Propagation Characteristics of Electric Dipole in Presence of Vegetation or Snow Layer. *IEEE Trans. Antennas and Propagation* **Nov. 2005**, 53, 3747–3756.
45. Sarabandi, K.; Koh, I. Effect of Canopy-Air Interface Roughness on HF-VHF Wave Propagation in Forest. *IEEE Trans. Antennas and Propagation*. **Feb. 2002**, 50, 111–121.
46. Lev-Ari, H.; Devaney, A. J. The Time-Reversal Technique Re-Interpreted: Subspace-Based Signal Processing For Multi-Static Target Location. *Proc. IEEE Sensor Array and Multichannel Signal Processing Workshop*, pp. 509–513, 2000.
47. Dagefu, F. T.; Sarabandi, K. Analysis and Modeling of Near-Ground Wave Propagation in the Presence of Building Walls. *IEEE Trans. Antennas and Propagation* **Jun. 2011**, 59 (6), 2368–2378.
48. Felsen, L. B.; Marcuvitz, N. *Radiation and Scattering of Waves*; NJ: Prentice-Hall, 1973.
49. Jordan, E. C.; Balmain, K. G. *Electromagnetic Waves and Radiating Systems*; Englewood Cliffs, NJ: Prentice-Hall, 1968.
50. Brekhovskikh, L. M. *Waves in Layered Media*; NY: Academic Press, 1960.
51. Tsang, L.; Kong, J. A.; Shin, R. T. *Theory of Microwave Remote Sensing*; NY: Wiley, 1985.

- 52. Kong, J. A.; Tsang, L.; Simmons, G. Geophysical Surface Probing With Radio-Frequency Interferometry. *IEEE Trans. Antennas and Propagation*. **Nov. 1974**, 22.
- 53. Chew, W. C. *Waves and Fields in Inhomogeneous Media*; NY: Van Nostrand Reinhold, 1990.
- 54. Beyer, J. B.; Prasad, S. N.; Becker, R. C.; Nordman, J. E.; Hohenwarter, G. K. MESFET Distributed Amplifier Design Guidelines. *IEEE Trans. Microw. Theory and Techniques* **Mar. 1984**, 32.
- 55. D. M. Pozar, *Microwave Engineering*; 2nd Ed., John Wiley and Sons, NY, 1997.

INTENTIONALLY LEFT BLANK.

Appendix A. Higher-Order Asymptotic Evaluation of Near-Earth Wave Propagation Characteristics of Electric Current Sources

Analytical formulations are derived for calculating the electric fields of a short dipole of arbitrary orientation situated above a finitely conducting ground plane in the presence of a dielectric layer. The discussion presented below is originally from the work by Liao (24). Note that specialized results for the half-space medium can be reached by, for example, setting the dielectric properties of the dielectric layer to those of air (or free space).

There are three primary configurations of interest, as a result of different combinations of the locations of the electric dipole and observation point. The dipole is assumed to be located on the z -axis with current moment vector $I_o \vec{l} = I_o (l_x \hat{x} + l_y \hat{y} + l_z \hat{z})$, and the observation point—identified with the usual cylindrical coordinates—is at (ρ, ϕ, z) . The xy -plane is aligned with the top of the dielectric layer, itself has thickness d . In the type of propagation problems considered here, for analysis restricted to the far field, it can be assumed that the magnitudes of z' , z , and d are much smaller than that of ρ —the radial distance between the dipole and the observation point. Also note that primed quantities are associated with the source, and the $\exp(-i\omega t)$ convention is assumed and suppressed in all the formulations.

A-1. Case 1 ($z' > 0$ and $z > 0$)

Consider the simple case when the source and observation points are both located in the upper layer (air) of a one-layer medium, the total electric field for a vertical dipole can be written as

$$E_{x,y,z}^{total} = E_{x,y,z}^{direct} + E_{x,y,z}^{scattered}. \quad (A-1)$$

Specifically, at grazing angle ($z' \ll \rho$ and $z \ll \rho$), each component of the field can be expanded as follows:

$$E_z^{total} = \frac{i\omega\mu_o I_o l_z e^{ik_o\rho}}{4\pi} \left\{ \frac{1}{\rho} + \frac{R_{TM}}{\rho} + \frac{C_{z,1}}{\rho^2} + \frac{C_{z,2}}{\rho^3} \dots \right\}, \quad (A-2)$$

$$E_x^{total} = \frac{i\omega\mu_o I_o l_z e^{ik_o\rho}}{4\pi} \cos\phi \left\{ \frac{(z'-z)}{\rho^2} - \frac{(z'+z)R_{TM}}{\rho^2} + \frac{C_{x,1}}{\rho^2} + \frac{C_{x,2}}{\rho^3} \dots \right\}, \quad (A-3)$$

$$E_y^{total} = \frac{i\omega\mu_o I_o l_z e^{ik_o\rho}}{4\pi} \sin\phi \left\{ \frac{(z'-z)}{\rho^2} - \frac{(z'+z)R_{TM}}{\rho^2} + \frac{C_{y,1}}{\rho^2} + \frac{C_{y,2}}{\rho^3} \dots \right\}. \quad (A-4)$$

The first term in the brackets is the direct field; the second term is the geometrical-optics reflection field; and the rest of the terms account for higher-order scattered fields—where the C s denote unknown factors. Since incidence is near grazing angle, it is easy to show that $R_{TM} \approx -1$, $(1-R_{TM}) \approx 2$, whereas $(1+R_{TM})$ is a small quantity proportional to $1/\rho$. For the z -component of the

field, it can be seen that the cancellation of the direct and geometrical-optics reflection term generates a $1/\rho^2$ resultant—which is of the same order as the next term in the expansion. Likewise, for the x and y components, the sum of the direct and geometrical-optics reflection also produces a term that is of the same order as the next higher-order term. Similar analysis can be applied to a horizontal dipole. Thus, when the source and observation points are close to the interface (incidence at grazing angle), it is apparent that an accurate description of the field components necessitates the derivation of the higher-order term that comes after the geometrical-optics reflection term.

The complete evaluation of the field quantities begins with the twofold integral form of the dyadic Green's function. A change of variable is applied to obtain the integration in terms of k_ρ and Bessel functions. In integral form, the resulting expressions—for which exact closed-form solutions do not exist—of the x , y , and z components of the scattered field are given in appendix B. Since numerical computation of these expressions is slow and formidable due to the presence of singularities and the highly oscillatory behavior of the Bessel function at large distance ρ , approximate asymptotic solutions are sought. In a standard procedure, Hankel's functions of the first and second kind are used in extending the limits of integration to negative and positive infinity (in k_ρ -plane). By transforming the integration over to the complex w -plane by the change of variable $k_\rho = k_o \sin w$, and then substituting the asymptotic form of the Hankel's function for large arguments, the integrand can be written in the following form—to which the standard method of steepest descents can be applied:

$$E_{ij}^s(\rho, \phi, z) = \frac{-k_o^3 \eta_o I_o l_i}{16\pi} \sqrt{\frac{2}{ik_o \rho \pi}} \int_{-\frac{\pi}{2} + i\infty}^{\frac{\pi}{2} - i\infty} f_{ij}(w) e^{q(w)} dw \quad (\text{A-5})$$

where subscripts $i, j = x, y$, or z and $q(w) = ik_o R \cos(w - w_s)$. The saddle point at $w = w_s$ is defined by $q'(w_s) = 0$; therefore

$$\sin w_s = \frac{\rho}{R}, \quad (\text{A-6})$$

$$\cos w_s = \frac{z + z'}{R}, \quad (\text{A-7})$$

$$R^2 = \rho^2 + (z + z')^2. \quad (\text{A-8})$$

After some manipulations and following the procedure of saddle point integration provided by Felsen and Marcuvitz (48), the j component of the saddle point contribution up to second order for a dipole pointed in the i direction can be written as

$$E_{ij}^{sp} = \frac{-k_o^3 \eta_o I_o l_i}{8\pi} e^{ik_o \rho} \cdot \left\{ f_{ij}(w_s) \left(\frac{1}{ik_o \rho} \right) + \frac{1}{2} \left[f_{ij}''(w_s) + \frac{f_{ij}(w_s)}{4} \right] \left(\frac{1}{ik_o \rho} \right)^2 \right\} \quad (\text{A-9})$$

where the two terms represent the first and second saddle point expansion terms. The first saddle point expansion term is the geometrical-optics reflection term and the second expansion term can be thought as a correction term that becomes dominant when the source and observation points are close to the interface. This correction term is also commonly known as the Norton wave (49). After some lengthy algebraic manipulations, expressions for $f_{ij}(w)$ of (A-9) can be shown to be the following:

$$f_{zx} = -\frac{2}{k_o} \sin^{\frac{3}{2}} w \cos w R_{TM}^{01}(w) \cos \phi, \quad (\text{A-10})$$

$$f_{zy} = -\frac{2}{k_o} \sin^{\frac{3}{2}} w \cos w R_{TM}^{01}(w) \sin \phi, \quad (\text{A-11})$$

$$f_{zz} = \frac{2}{k_o} \sin^{\frac{5}{2}} w R_{TM}^{01}(w), \quad (\text{A-12})$$

$$f_{xx,yy} = \sin^{\frac{1}{2}} w \cos w [R_-(w) \mp R_+(w) \cos(2\phi)], \quad (\text{A-13})$$

$$f_{xy,yx} = -\sin^{\frac{1}{2}} w \cos w R_+(w) \sin(2\phi), \quad (\text{A-14})$$

$$f_{xz} = \frac{2}{k_o} \sin^{\frac{3}{2}} w \cos w R_{TM}^{01}(w) \cos \phi, \quad (\text{A-15})$$

$$f_{yz} = \frac{2}{k_o} \sin^{\frac{3}{2}} w \cos w R_{TM}^{01}(w) \sin \phi. \quad (\text{A-16})$$

The mixed reflection coefficient, which is required for an x or y -directed dipole, is defined as

$$R_{\pm}(w) = \frac{R_{TE}^{01}(w)}{k_o \cos w} \pm \frac{\cos w R_{TM}^{01}(w)}{k_o}. \quad (\text{A-17})$$

The TE and TM reflection coefficients are of the standard form:

$$R_{TE}^{mn}(w) = \frac{\sqrt{\epsilon_{rm} - \sin^2 w} - \sqrt{\epsilon_{rn} - \sin^2 w}}{\sqrt{\epsilon_{rm} - \sin^2 w} + \sqrt{\epsilon_{rn} - \sin^2 w}}, \quad (\text{A-18})$$

$$R_{TM}^{mn}(w) = \frac{\epsilon_{rn} \sqrt{\epsilon_{rm} - \sin^2 w} - \epsilon_{rm} \sqrt{\epsilon_{rn} - \sin^2 w}}{\epsilon_{rn} \sqrt{\epsilon_{rm} - \sin^2 w} + \epsilon_{rm} \sqrt{\epsilon_{rn} - \sin^2 w}}. \quad (\text{A-19})$$

The appearance of branch points at $w_b = \pm \sin^{-1} \sqrt{\epsilon_{r1}}$ entails the use of a two-sheeted Riemann surface in representing the w -plane; in order to satisfy the radiation condition, the path of integration of (A-5) is restricted to lie on the upper sheet ($\text{Im} \sqrt{\epsilon_{r1} - \sin^2 w} > 0$). The branch cut defined by $w_b = \sin^{-1} \sqrt{\epsilon_{r1}}$ may be crossed by the steepest descent path and its contribution to the integral can be included by adding the following to the saddle point contribution (48):

$$E_{ij}^b = \left(\frac{-k_o \eta_o I_o l_i}{8\pi} \right) \left(\sqrt{-2ie}^{-\frac{3}{2}i \arg(-ik_o \sqrt{1-\varepsilon_{r1}})} \right) \left(\frac{e^{ik_1 \rho + ik_o \sqrt{1-\varepsilon_{r1}}(z+z')}}{\sqrt{\rho} |\rho \sqrt{1-\varepsilon_{r1}} - (z+z') \sqrt{\varepsilon_{r1}}|^{\frac{3}{2}}} \right) \cdot \lim_{w \rightarrow w_b} \sqrt{w - w_b} f'_{ij}(w) \quad (\text{A-20})$$

It can be readily verified (48, 50) that the poles of the integrand in equation A-5 are not intercepted as the original integration path deforms to the steepest descent path. Depending on the permittivity of the lower medium (ε_{r1}), these poles (the zeros of the denominator of the reflection coefficients in equations A-18 and A-19) may move into the vicinity of the saddle point; thus, the poles may come into effect indirectly and must be taken into account by carrying out a modified saddle point integration method. Simulation results, however, show that the ordinary saddle point integration as used here is sufficient for predicting the field contributions in the far field. The total field is then the sum of the direct, saddle point, and branch cut contributions:

$$E_{ij} = E_{ij}^d + E_{ij}^{sp} + U(w_s - \theta_b) E_{ij}^b \quad (\text{A-21})$$

where $\theta_b = \text{Re}(w_b) - \cos^{-1} \text{sech}[\text{Im}(w_b)]$, and $U(\cdot)$ is the Heaviside step function. Calculation of equation A-20 can be quite involved, but note that the branch cut contribution decays exponentially with ρ since the wave number k_1 is complex; therefore, at large ρ , the branch cut contribution can be considered as negligible.

For a two-layer medium, to account for higher-order reflections that are transmitted into and then emerging from the dielectric layer, the total reflection coefficient is modified as follows (51):

$$R_p(w) = R_p^{01} + \sum_{u=1}^{\infty} T_p^{01} (R_p^{12})^u (R_p^{10})^{u-1} T_p^{10} e^{i2udk_o \sqrt{\varepsilon_{r1} - \sin^2 w}}. \quad (\text{A-22})$$

Using the relations

$$R_p^{mm} = -R_p^{nm} \text{ and } T_p^{mm} = 1 + R_p^{nm}, \quad (\text{A-23})$$

Equation A-22 can be re-written as

$$R_p(w) = \frac{R_p^{01} + R_p^{12} e^{i2dk_o \sqrt{\varepsilon_{r1} - \sin^2 w}}}{1 + R_p^{01} R_p^{12} e^{i2dk_o \sqrt{\varepsilon_{r1} - \sin^2 w}}}. \quad (\text{A-24})$$

The subscribe “ P ” is a place holder for the polarization—either TE or TM. The saddle point contribution for each higher-order reflection ($u = 1, 2, \dots \infty$) in the summation series of equation A-22 can be evaluated by using equation A-9 after replacing the reflection coefficient term in $f_{ij}(w)$ with $T_p^{01} (R_p^{12})^u (R_p^{10})^{u-1} T_p^{10} e^{i2udk_o \sqrt{\varepsilon_{r1} - \sin^2 w}}$. Note that the higher-order reflections lead to higher-order poles for the terms in the summation series of equation A-22. Although they are still located outside of the steepest descent path, these poles are close enough that—at higher orders—they demand a more refined saddle point integration method even when ρ is relatively large. In order to circumvent this difficulty, calculations are made by following the normal mode

approach in which the total aggregate reflection coefficient in equation A-24 is inserted into equations A-10–A-16 as a whole rather than as individuals in a series. This approach leads to satisfactory results in the far field even if we are ignoring the pole contributions—which are now supplied by the zeros of the denominator in equation A-24 and must be located through numerical methods before their contributions can be included using a standard technique (48). These pole contributions, depending on their locations on the complex plane, represent either distinct surface-wave modes or leaky modes—both of which become less significant as the distance between source and observation points increases (48, 52). Also note that in the two-layer case there are branch points only at $w_b = \pm \sin^{-1} \sqrt{\epsilon_{r2}}$ since the expression in equation A-24 can be shown to be an even function of $\sqrt{\epsilon_{r1} - \sin^2 w}$. The branch point that can be intercepted is at $w_b = \sin^{-1} \sqrt{\epsilon_{r2}}$, but since medium 2 (the ground layer) is highly lossy, the branch cut contribution falls off asymptotically according to $\sim e^{ik_2 \rho}$ and, hence, rapidly becomes much smaller than the algebraically decaying saddle point contribution.

A-2. Case 2 ($-\mathbf{d} < \mathbf{z}' < \mathbf{0}$ and $\mathbf{z} > \mathbf{0}$)

Exact formulations for this case have been derived and can be found in appendix B. Proceeding through the same procedure as before, the method of steepest descents is employed in obtaining the integral after transforming the integration to the w -plane. Multiple reflections occurring within the dielectric layer can be accommodated by defining the total transmission coefficient as the following:

$$T_p^{up}(w) = T_p^{10} \sum_{u=0}^{\infty} (R_p^{10} R_p^{12})^u e^{i2udk_o \sqrt{\epsilon_{r1} - \sin^2 w}} = \frac{T_p^{10}}{1 + R_p^{01} R_p^{12} e^{i2dk_o \sqrt{\epsilon_{r1} - \sin^2 w}}} \quad (\text{A-25})$$

and

$$T_p^{down}(w) = T_p^{up} R_p^{12}. \quad (\text{A-26})$$

The definition of equation A-26 differs from that of equation A-25 in that the former expression applies to waves containing an initial bounce off the dielectric layer/ground interface. It can be shown that the transmitted field E_{ij} for each order u can be written as

$$E_{ij,u}(\rho, \phi, z) = \frac{-k_o^3 \eta_o I_o l_i}{16\pi} \sqrt{\frac{2}{ik_o \rho \pi}} \int_{-\frac{\pi}{2} + i\infty}^{\frac{\pi}{2} - i\infty} f_{ij,u}(w) e^{q(w)} dw \quad (\text{A-27})$$

where

$$q(w) = ik_o(\rho \sin w + z \cos w) \approx ik_o \rho \cos(w - w_s) \quad (\text{A-28})$$

and the saddle point can be approximately defined by

$$\cos w_s \approx \frac{z}{\rho}. \quad (\text{A-29})$$

The set of $f_{ij,u}(w)$ for an arbitrary oriented dipole can be shown to take the following forms:

$$f_{zx,u} = -\frac{2}{k_o} \frac{\sin^{\frac{3}{2}} w \cos^2 w}{\sqrt{\epsilon_{r1} - \sin^2 w}} \cos \phi \left\{ T_{TM,u}^{up} e^{c_{up}(w)} + T_{TM,u}^{down} e^{c_{down}(w)} \right\}, \quad (\text{A-30})$$

$$f_{zy,u} = -\frac{2}{k_o} \frac{\sin^{\frac{3}{2}} w \cos^2 w}{\sqrt{\epsilon_{r1} - \sin^2 w}} \sin \phi \left\{ T_{TM,u}^{up} e^{c_{up}(w)} + T_{TM,u}^{down} e^{c_{down}(w)} \right\}, \quad (\text{A-31})$$

$$f_{zz,u} = \frac{2}{k_o} \frac{\sin^{\frac{5}{2}} w \cos w}{\sqrt{\epsilon_{r1} - \sin^2 w}} \left\{ T_{TM,u}^{up} e^{c_{up}(w)} + T_{TM,u}^{down} e^{c_{down}(w)} \right\}, \quad (\text{A-32})$$

$$f_{xx,u} = \sin^{\frac{1}{2}} w \cos w \left\{ \left[T_+^{up} - T_-^{up} \cos(2\phi) \right] e^{c_{up}(w)} + \left[T_-^{down} - T_+^{down} \cos(2\phi) \right] e^{c_{down}(w)} \right\}, \quad (\text{A-33})$$

$$f_{yy,u} = \sin^{\frac{1}{2}} w \cos w \left\{ \left[T_+^{up} + T_-^{up} \cos(2\phi) \right] e^{c_{up}(w)} + \left[T_-^{down} + T_+^{down} \cos(2\phi) \right] e^{c_{down}(w)} \right\}, \quad (\text{A-34})$$

$$f_{xy,u} = f_{yx,u} = -\sin^{\frac{1}{2}} w \cos w \sin(2\phi) \left\{ T_-^{up} e^{c_{up}(w)} + T_+^{down} e^{c_{down}(w)} \right\}, \quad (\text{A-35})$$

$$f_{xz,u} = -\frac{2}{k_o} \sin^{\frac{3}{2}} w \cos w \cos \phi \left\{ T_{TM,u}^{up} e^{c_{up}(w)} - T_{TM,u}^{down} e^{c_{down}(w)} \right\}, \quad (\text{A-36})$$

$$f_{yz,u} = -\frac{2}{k_o} \sin^{\frac{3}{2}} w \cos w \sin \phi \left\{ T_{TM,u}^{up} e^{c_{up}(w)} - T_{TM,u}^{down} e^{c_{down}(w)} \right\}, \quad (\text{A-37})$$

in which

$$c_{up}(w) = ik_o \sqrt{\epsilon_{r1} - \sin^2 w} |z|, \quad (\text{A-38})$$

$$c_{down}(w) = ik_o \sqrt{\epsilon_{r1} - \sin^2 w} (z' + 2d). \quad (\text{A-39})$$

The designations “*up*” and “*down*” differentiate waves that are initially propagating upward and downward from the source. The mixed transmission coefficients have been written in the following form:

$$T_{\pm}^{up}(w) = \frac{T_{TE,u}^{up}}{k_o \sqrt{\epsilon_{r1} - \sin^2 w}} \pm \frac{T_{TM,u}^{up} \cos w}{k_o}, \quad (\text{A-40})$$

$$T_{\pm}^{down}(w) = \frac{T_{TE,u}^{down}}{k_o \sqrt{\epsilon_{r1} - \sin^2 w}} \pm \frac{T_{TM,u}^{down} \cos w}{k_o}. \quad (\text{A-41})$$

In the formulations above, $T_{P,u}^{up}$ and $T_{P,u}^{down}$ are the individual terms in the infinite series of equations A-25 and A-26, respectively. Instead of computing each order of transmission separately, the saddle point evaluation of equation A-27 can be carried out using equation A-9 as before by means of the normal mode approach—in which now the aggregate transmission coefficients in equations A-25 and A-26 are substituted into $f_{ij}(w)$ as one term. The difficulty mainly lies in taking the double derivative of $f_{ij}(w)$, but this can be overcome with the help of a symbolic math software. When the source and observation points are located in the vicinity of the interface, it is seen that both the first and second term in the saddle point expansion fall off as $1/\rho^2$; thus, as in Case 1, both expansion terms are necessary for accurate representation of the total field.

It is seen that the sign of the term $\sqrt{\varepsilon_{r1} - \sin^2 w}$ has no effect on the final result in computing the integral in equation A-27; therefore, once again, the function $f_{ij}(w)$ is an even function of $\sqrt{\varepsilon_{r1} - \sin^2 w}$ and the only branch points on the complex w -plane are attributed to the term $\sqrt{\varepsilon_{r2} - \sin^2 w}$. (As a matter of fact, for general stratified media problems, in the normal mode approach, the branch points on the k_ρ plane are supplied only by the first and last layer (53). The branch points of the first layer can be eliminated—as it has been done here—by translating the calculation onto the w -plane after the change of variable $k_\rho = k_o \sin w$. Thus, on the w -plane, the only branch points remaining are due to the last layer in the stratification.) Similar to case 1, calculations are much simplified by ignoring contributions from the branch cut and the poles (which are provided by the zeros of the denominator of equations A-25 and A-26). In the far field, this claim is justified since the saddle point contribution becomes the only dominant field component.

A-3. Case 3 ($-d < z' < 0$ and $-d < z < 0$)

As it has been shown in reference 45, when both the source and observation points are located inside medium 2, the direct and saddle point contributions decay exponentially as a function of the radial distance ρ since their propagation takes place in a lossy medium. The dominant contribution to the total field, as it turns out, comes from a branch cut contribution. Although a modal analysis can be used, a ray tracing approach provides a more insightful interpretation for this case. In the ray tracing approach, the effective reflection coefficient is expanded as a series before asymptotic evaluation is carried out separately for each term. In such an approach, both medium 1 and medium 2 would furnish branch cut contributions on the w -plane since now—for each individual order of reflection—the integrand in the field integral is no longer an even function of $\sqrt{\varepsilon_{r1} - \sin^2 w}$. Discarding the branch cut contribution arising from the branch point at $w_b = \sin^{-1} \sqrt{\varepsilon_{r2}}$ for the reason mentioned earlier, the only relevant and significant contribution, in the far field, comes from the branch cut contribution due to the branch point at $w_b = \sin^{-1} \sqrt{\varepsilon_{r1}}$.

This branch cut contribution, which now no longer undergoes exponential decay, can be interpreted as a wave from the source that radiates upward to the dielectric/air interface at critical angle and then propagates along the interface (in air) before reaching the observation point at critical angle again. Since the majority of the propagation takes place in air, this field

component—which has been labeled as the “lateral” wave—does not suffer the large path loss experienced by the direct and saddle point contributions. Through standard branch cut integration techniques, the three lowest orders of lateral waves have been derived in reference 45 and are expressed in matrix form as the following ($z' > z$):

$$\vec{E}^b = \frac{-i\eta_1}{2\pi(1-1/\epsilon_{r1})^{\frac{1}{4}}} \frac{e^{ik_o\rho}}{\sqrt{\rho}} \left\{ \frac{e^{ik_1\sqrt{1-1/\epsilon_{r1}}(|z'|+|z|)}}{\left[\sqrt{1/\epsilon_{r1}}(|z'|+|z|)-\rho\sqrt{1-1/\epsilon_{r1}}\right]^{\frac{3}{2}}} \vec{A} + \right. \\ \left. \frac{e^{ik_1\sqrt{1-1/\epsilon_{r1}}(2d-|z'|+|z|)}}{\left[\sqrt{1/\epsilon_{r1}}(2d-|z'|+|z|)-\rho\sqrt{1-1/\epsilon_{r1}}\right]^{\frac{3}{2}}} \vec{A} \cdot \vec{R} + \right. \\ \left. \frac{e^{ik_1\sqrt{1-1/\epsilon_{r1}}(2d+|z'|-|z|)}}{\left[\sqrt{1/\epsilon_{r1}}(2d+|z'|-|z|)-\rho\sqrt{1-1/\epsilon_{r1}}\right]^{\frac{3}{2}}} \vec{A} \cdot \vec{R} \right\} \cdot I_o \vec{l} \quad (\text{A-42})$$

where \vec{A} and \vec{R} are symmetric dyads defined in reference 45. The first term in equation A-42 represents the direct lateral wave contribution; the second term is the contribution of the lateral wave generated from the image of the source in the ground plane; and the third term is the contribution of the direct lateral wave that has been reflected from the ground plane before reaching the observation point. It is seen that the lateral waves, and hence the total field, decreases as $1/\rho^2$ —which is the same asymptotic behavior observed for the first two cases. For further details on the derivation and verification of equation A-42, the reader is referred to reference 45.

Although the transmitter has been restricted to an electric dipole throughout this work, extension to an arbitrary radiating source can be made by noting that the asymptotic form of the Green's function for each of the three cases discussed is related to the derived expressions for the field components by a simple constant:

$$\vec{\vec{G}}(\vec{r}', \vec{r}) = \frac{1}{i\omega\mu_o} \begin{bmatrix} E_{xx} & E_{yx} & E_{zx} \\ E_{xy} & E_{yy} & E_{zy} \\ E_{xz} & E_{yz} & E_{zz} \end{bmatrix}. \quad (\text{A-43})$$

Therefore, once the current distribution of an arbitrary source is known, an approximation to the far-field pattern can be easily computed. Also, upon application of the reciprocity principle, it is straightforward to verify that

$$\vec{\vec{G}}(\vec{r}, \vec{r}') = \vec{\vec{G}}(\vec{r}', \vec{r})^T \quad (\text{A-44})$$

where the superscript “ T ” indicates the transpose operation. Simply by using the relation stated in equation A-44, the formulations can be extended to other standard configurations not explicitly treated above—for example, the dipole is located in air while the observation point is located inside the dielectric layer.

A comparison of the asymptotic solution with the exact solution is shown in figures A-1 and A-2—for a half-space radiation problem.

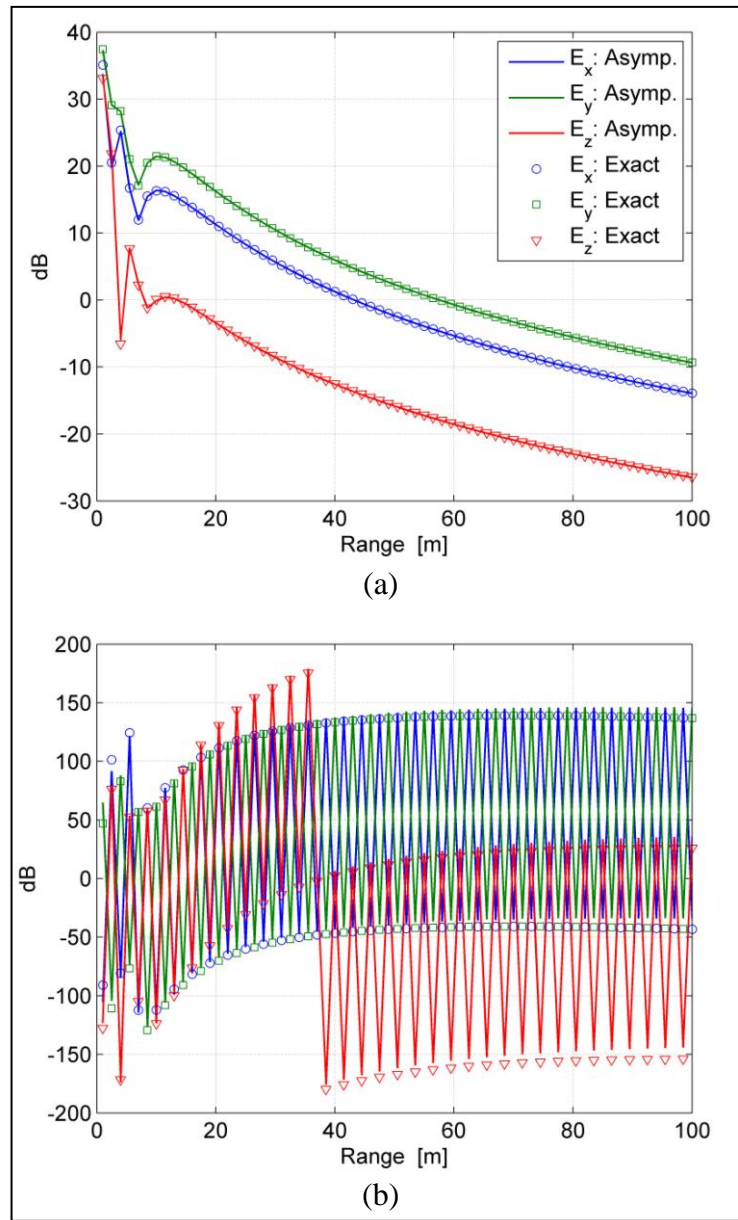


Figure A-1. (a) Magnitude and (b) phase of the electric fields of a horizontal electric dipole as a function of range. The dipole is located on the z -axis at a 2-m height above the ground and the observation point is at a 1.7-m height along a radial line at $\phi = 30^\circ$. Ground properties: $\epsilon_r' = 4$, $\sigma_d = 10$ mS/m, and $f = 300$ MHz.

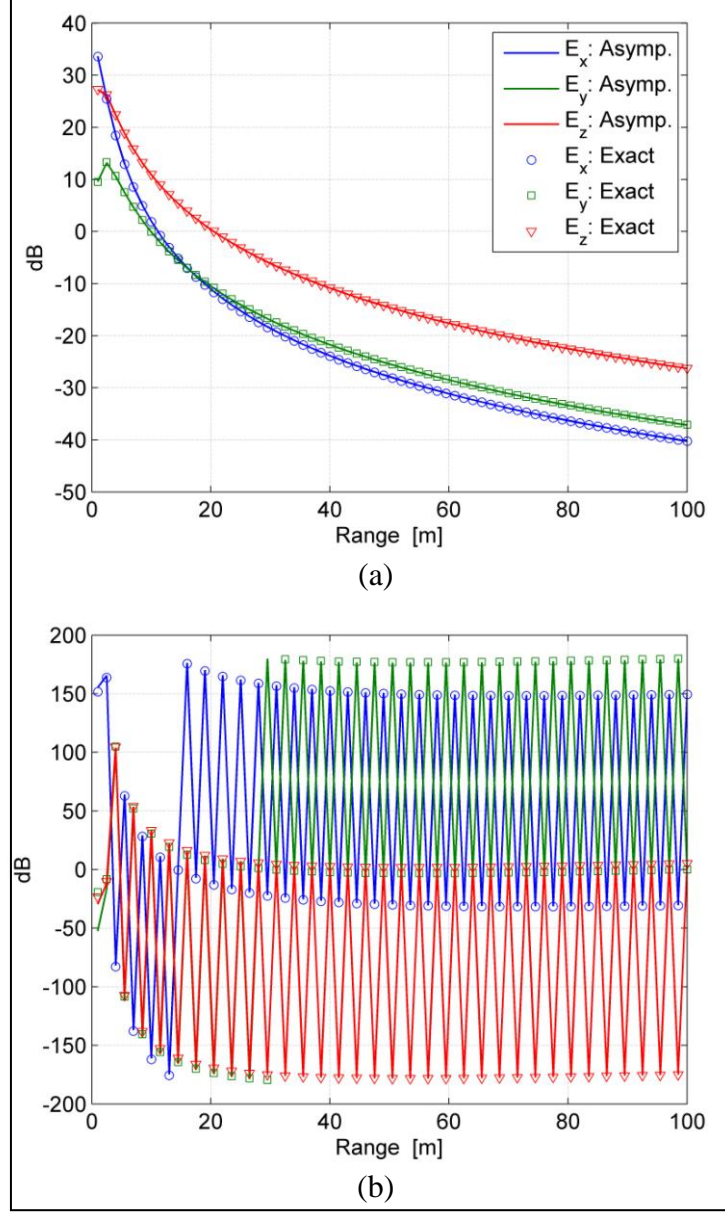


Figure A-2. (a) Magnitude and (b) phase of the electric fields of a horizontal electric dipole as a function of range. The dipole is buried in the ground at a 10-cm depth and the observation point is at a 1.7-m height along a radial line at $\phi = 30^\circ$. Ground properties: $\epsilon_r' = 4$, $\sigma_d = 10$ mS/m, and $f = 300$ MHz.

Appendix B. Sommerfeld Integrals for Electric Current Sources

Exact integral representations of the radiation from an electric dipole located in the presence of a two-layer infinite medium are presented below. The details of the derivation can be found in the work by Liao (24).

B-1. Integral Solutions for Case 1 ($z' > 0$ and $z > 0$)

Exact expressions for the electric field of a dipole radiating in the presence of a two-layer medium are derived from the dyadic Green's function. If the arbitrarily oriented dipole is located on the z -axis at $(0, 0, z')$ with the current moment vector $I_o \vec{l} = I_o (l_x \hat{x} + l_y \hat{y} + l_z \hat{z})$, it can be shown that—for Case 1—the general equation for the scattered electric field at observation point (ρ, ϕ, z) with $z' > z$ can be written as

$$E_{ij}^s = -\frac{\omega \mu_o I_o l_i}{8\pi} \int_0^\infty f_{ij}(k_\rho) e^{ik_{oz}(z+z')} dk_\rho \quad (\text{B-1})$$

where the function in the integrand is dependent upon the dipole orientation and the field component of interest (x , y , or z):

$$f_{zx}(k_\rho) = \frac{-2ik_\rho^2}{k_o^2} R_{TM}(k_\rho) J_1(k_\rho \rho) \cos \phi, \quad (\text{B-2})$$

$$f_{zy}(k_\rho) = \frac{-2ik_\rho^2}{k_o^2} R_{TM}(k_\rho) J_1(k_\rho \rho) \sin \phi, \quad (\text{B-3})$$

$$f_{zz}(k_\rho) = \frac{2k_\rho^3}{k_{oz} k_o^2} R_{TM}(k_\rho) J_0(k_\rho \rho), \quad (\text{B-4})$$

$$f_{xx,yy}(k_\rho) = k_\rho [R_-(k_\rho) J_0(k_\rho \rho) \pm R_+(k_\rho) J_2(k_\rho \rho) \cos(2\phi)], \quad (\text{B-5})$$

$$f_{xy,yx}(k_\rho) = k_\rho R_+(k_\rho) J_2(k_\rho \rho) \sin(2\phi), \quad (\text{B-6})$$

$$f_{xz}(k_\rho) = \frac{2ik_\rho^2}{k_o^2} R_{TM}(k_\rho) J_1(k_\rho \rho) \cos \phi, \quad (\text{B-7})$$

$$f_{yz}(k_\rho) = \frac{2ik_\rho^2}{k_o^2} R_{TM}(k_\rho) J_1(k_\rho \rho) \sin \phi. \quad (\text{B-8})$$

The total reflection coefficient is given by

$$R_p = R_p^{01} + T_p^{01} T_p^{10} \sum_{u=1}^{\infty} (R_p^{10})^{u-1} (R_p^{12} e^{i2k_{1z}d})^u = R_p^{01} + \frac{[1 - (R_p^{01})^2] R_p^{12} e^{i2k_{1z}d}}{1 + R_p^{01} R_p^{12} e^{i2k_{1z}d}} = \frac{R_p^{01} + R_p^{12} e^{i2k_{1z}d}}{1 + R_p^{01} R_p^{12} e^{i2k_{1z}d}} \quad (\text{B-9})$$

and the mixed reflection coefficient is

$$R_{\pm}(k_{\rho}) = \frac{R_{TE}(k_{\rho})}{k_{oz}} \pm \frac{R_{TM}(k_{\rho})k_{oz}}{k_o^2} \quad (B-10)$$

where the simple reflection coefficients for a wave going from layer m to layer n are the following:

$$R_{TE}^{mn} = \frac{k_{mz} - k_{nz}}{k_{mz} + k_{nz}}, \quad (B-11)$$

$$R_{TM}^{mn} = \frac{\varepsilon_{rn}k_{mz} - \varepsilon_{rm}k_{nz}}{\varepsilon_{rn}k_{mz} + \varepsilon_{rm}k_{nz}}. \quad (B-12)$$

The wavenumber is represented by k_u ($u = 0, 1$, or 2) and

$$k_{uz} = \sqrt{k_u^2 - k_{\rho}^2}. \quad (B-13)$$

The direct field must be added to the scattered field to obtain the total field. If $z' < z$, the relation in equation A-44 should be applied.

B-2. Integral Solutions for Case 2 ($-d < z' < 0$ and $z > 0$)

When the dipole is inside the dielectric layer and the observation point is in air, the derivation for the total field is more complicated but is not much different from that of the first case. Simple manipulations of the dyadic Green's function give the transmitted field as

$$E_{ij} = -\frac{\omega\mu_o I_o l_i}{8\pi} \int_0^{\infty} f_{ij}(k_{\rho}) e^{ik_{oz}z} dk_{\rho} \quad (B-14)$$

where the set of $f_{ij}(k_{\rho})$ functions can be shown to be

$$f_{zx}(k_{\rho}) = \frac{-2ik_{\rho}^2 k_{oz}}{k_o^2 k_{1z}} [T_{TM}^{up} e^{ik_{1z}|z|} + T_{TM}^{down} e^{ik_{1z}(2d+z')}] J_1(k_{\rho}\rho) \cos\phi, \quad (B-15)$$

$$f_{zy}(k_{\rho}) = \frac{-2ik_{\rho}^2 k_{oz}}{k_o^2 k_{1z}} [T_{TM}^{up} e^{ik_{1z}|z|} + T_{TM}^{down} e^{ik_{1z}(2d+z')}] J_1(k_{\rho}\rho) \sin\phi, \quad (B-16)$$

$$f_{zz}(k_{\rho}) = \frac{2k_{\rho}^3}{k_{1z} k_o^2} [T_{TM}^{up} e^{ik_{1z}|z|} + T_{TM}^{down} e^{ik_{1z}(2d+z')}] J_0(k_{\rho}\rho), \quad (B-17)$$

$$f_{xx,yy}(k_{\rho}) = k_{\rho} \{ [T_{+}^{up} e^{ik_{1z}|z|} + T_{-}^{down} e^{ik_{1z}(2d+z')}] J_0(k_{\rho}\rho) \\ \pm [T_{-}^{up} e^{ik_{1z}|z|} + T_{+}^{down} e^{ik_{1z}(2d+z')}] J_2(k_{\rho}\rho) \cos(2\phi) \}, \quad (B-18)$$

$$f_{xy,yx}(k_{\rho}) = k_{\rho} \{ T_{-}^{up} e^{ik_{1z}|z|} + T_{+}^{down} e^{ik_{1z}(2d+z')} \} J_2(k_{\rho}\rho) \sin(2\phi), \quad (B-19)$$

$$f_{xz}(k_{\rho}) = \frac{2ik_{\rho}^2}{k_o^2} [-T_{TM}^{up} e^{ik_{1z}|z|} + T_{TM}^{down} e^{ik_{1z}(2d+z')}] J_1(k_{\rho}\rho) \cos\phi, \quad (B-20)$$

$$f_{yz}(k_{\rho}) = \frac{2ik_{\rho}^2}{k_o^2} [-T_{TM}^{up} e^{ik_{1z}|z|} + T_{TM}^{down} e^{ik_{1z}(2d+z')}] J_1(k_{\rho}\rho) \sin\phi. \quad (B-21)$$

The various transmission coefficients are defined below:

$$T_{\pm}^{up}(k_{\rho}) = \frac{T_{TE}^{up}(k_{\rho})}{k_{1z}} \pm \frac{T_{TM}^{up}(k_{\rho})k_{oz}}{k_o^2}, \quad (\text{B-22})$$

$$T_{\pm}^{down}(k_{\rho}) = \frac{T_{TE}^{down}(k_{\rho})}{k_{1z}} \pm \frac{T_{TM}^{down}(k_{\rho})k_{oz}}{k_o^2}, \quad (\text{B-23})$$

$$T_p^{up} = T_p^{10} \sum_{u=0}^{\infty} (R_p^{10} R_p^{12} e^{i2k_{1z}d})^u = \frac{T_p^{10}}{1 + R_p^{01} R_p^{12} e^{i2k_{1z}d}}, \quad (\text{B-24})$$

$$T_p^{down} = R_p^{12} T_p^{10} \sum_{u=0}^{\infty} (R_p^{10} R_p^{12} e^{i2k_{1z}d})^u = \frac{R_p^{12} T_p^{10}}{1 + R_p^{01} R_p^{12} e^{i2k_{1z}d}}. \quad (\text{B-25})$$

INTENTIONALLY LEFT BLANK.

Appendix C. Traveling-Wave Amplifier Design

Detailed procedure for the design of the metal semiconductor field effect transistor (MESFET) distributed amplifier employed in the simulation example of section 3.1 is outlined. First, a simplified small-signal model is derived, then preliminary designs are achieved by following the guidelines reported by Beyer et al. (54). From these preliminary designs, it is shown that the optimum amplifier should be a two-stage network ($n = 2$).

The amplifier is based on the *TGF-4350EPU* transistor from TriQuint. In a standard procedure, the small-signal characteristics of the device must be obtained at the beginning of the design process. The S -parameters of the transistor are calculated using the full small-signal model (figure C-1) provided by TriQuint.

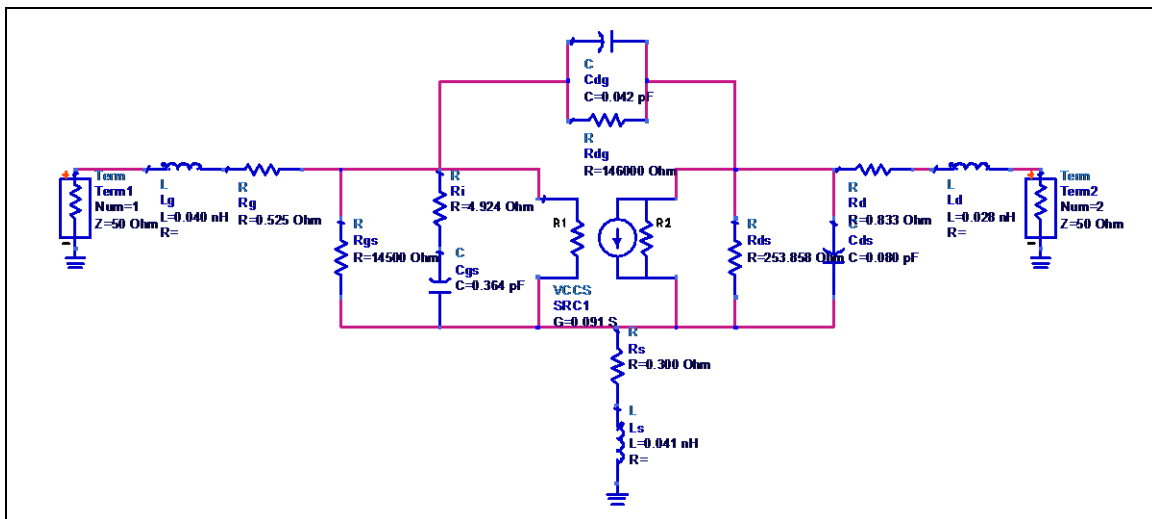


Figure C-1. TriQuint small-signal model for transistor.

Next, a simplified small-signal model for the transistor is derived using a circuit simulator and is shown in figure C-2.

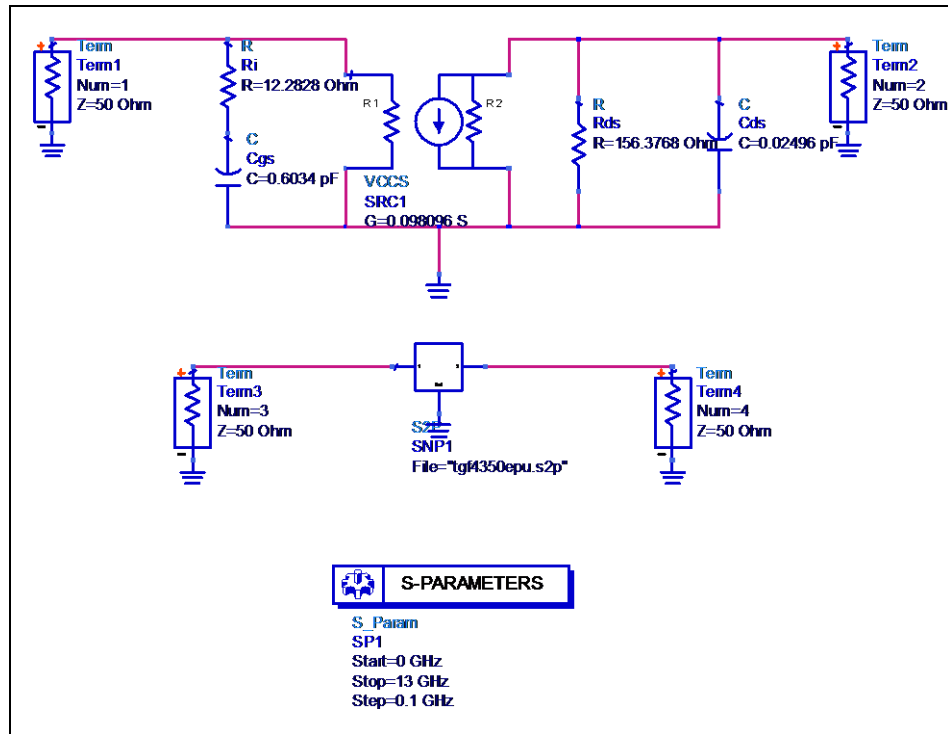


Figure C-2. Simulation with simplified small-signal model.

The S -parameters of the simplified model are compared to those of the original complete model in figure C-3. It can be seen that there is a very good match for S_{11} and S_{21} ; there is a poor match for S_{22} since the original model contains parasitics that cannot be included in the simplified model; also note that the simplified model is unilateral.

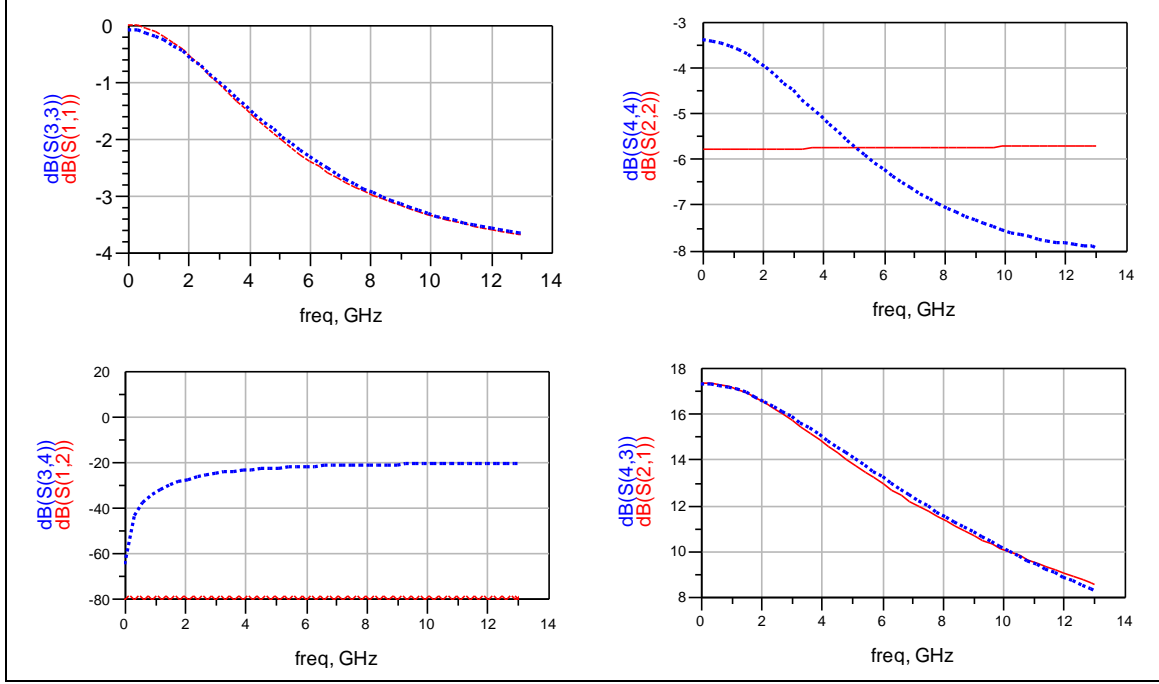


Figure C-3. Comparison between full small-signal model (blue lines) and simplified small-signal model (red lines).

Using the values of the components in the simplified model, the design procedure outlined by Beyer et al. is followed. The initial design curves are plotted in figure C-4. For a 50Ω design, the cutoff frequency can be calculated with the following relations (54):

$$R_{01} = \frac{1}{\pi f_c C_{gs}} = R_{02} = \frac{1}{\pi f_c (C_{ds} + C_p)} = 50 \Omega . \quad (C-1)$$

Since C_{gs} is fixed, f_c must be equal to 10.55 GHz. It is easily seen that, to equalize the impedance of the gate and drain lines, an additional capacitance, $C_p = 0.5784$ pF, must be added to the drain. The required inductances on the gate and drain lines are then calculated as (54)

$$f_c = \frac{1}{\pi \sqrt{L_g C_{gs}}} = \frac{1}{\pi \sqrt{L_d (C_{ds} + C_p)}} \rightarrow L_g = L_d = 1.5085 \text{ nH} . \quad (C-2)$$

As it is done in reference 54, the image terminations are realized by using m -derived filter half sections (55) at both ends of the lines. The form of the termination is shown in figure C-5. The values of the inductors and capacitor are

$$L_m = \frac{m L_g}{2} = 0.4526 \text{ nH} ; \quad (C-3)$$

$$L_{m2} = \frac{L_g (1 - m^2)}{2m} = 0.8045 \text{ nH} ; \quad (C-4)$$

$$C_m = \frac{mC_{gs}}{2} = 0.1810 \text{ pF}; \quad (\text{C-5})$$

where, as shown in reference 55, the optimum value for m is 0.6.

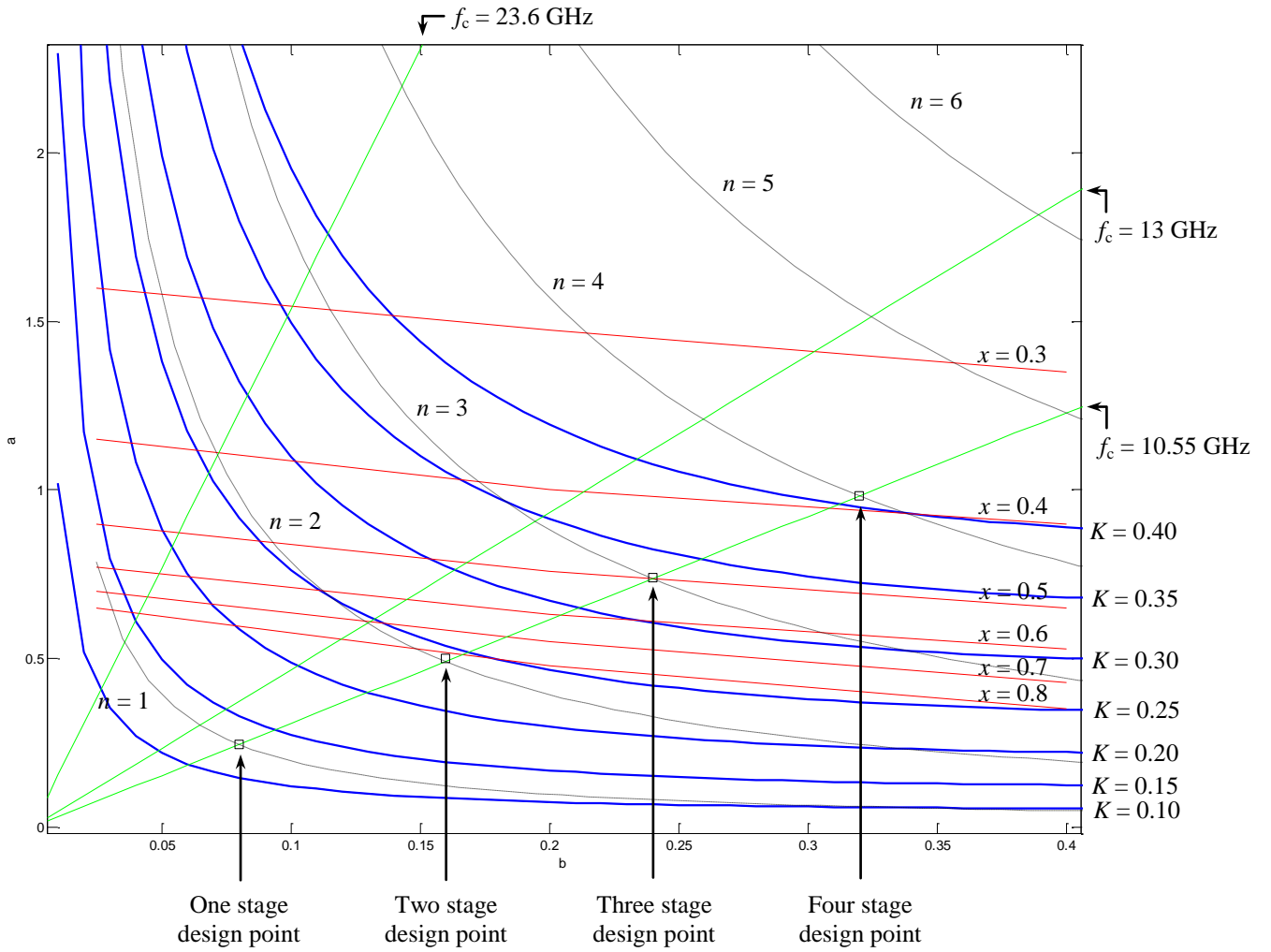


Figure C-4. Design curves.

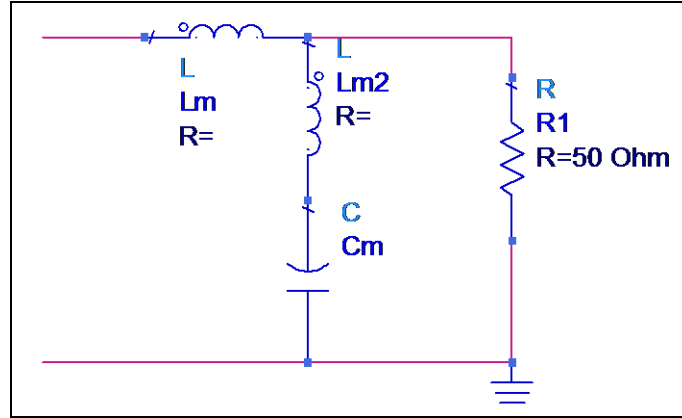


Figure C-5. Line termination.

Once the small-signal model of the device and the values of the different components (L_g , L_d , C_p , L_m , L_{m2} , C_m) in the amplifier network are defined, the preliminary design is carried out in the circuit simulator. An example of the preliminary design using lumped-elements is shown in figure C-6 (for $n = 2$). The schematics of the distributed designs—for $n = 1, 2, 3, 4$ —are also derived (figure C-7 shows the design for $n = 2$). In each of these preliminary distributed designs, inductors are replaced by short transmission lines with parameters $Z_o = 100 \, \Omega$ and $L = Z_o l / \lambda_g f$; and lumped-element capacitors are still used (but can be replaced with MIM capacitors later in the design process). Bias is done with an ideal DC-feed inductor and DC-block capacitors are added. Also, note that the actual (not simplified) small-signal model is used for the transistor in these designs—all of which are over a gallium arsenide (GaAs) substrate. After making the above changes, the component values of each circuit are tuned to maximize the gain while keeping its variation less than 1 dB over the entire bandwidth. It is seen that a bandwidth of 10 GHz can be realized with a design using $n = 2$. With f_c fixed, a larger number of devices increases the gain but reduces the bandwidth, while a smaller number of devices leads to a smaller gain but wider bandwidth—this is consistent with the trends displayed in figure C-4. Consequently, from a survey of these preliminary designs, with the constraint that the bandwidth equals 10 GHz, it is concluded that the optimum number of devices is $n = 2$.

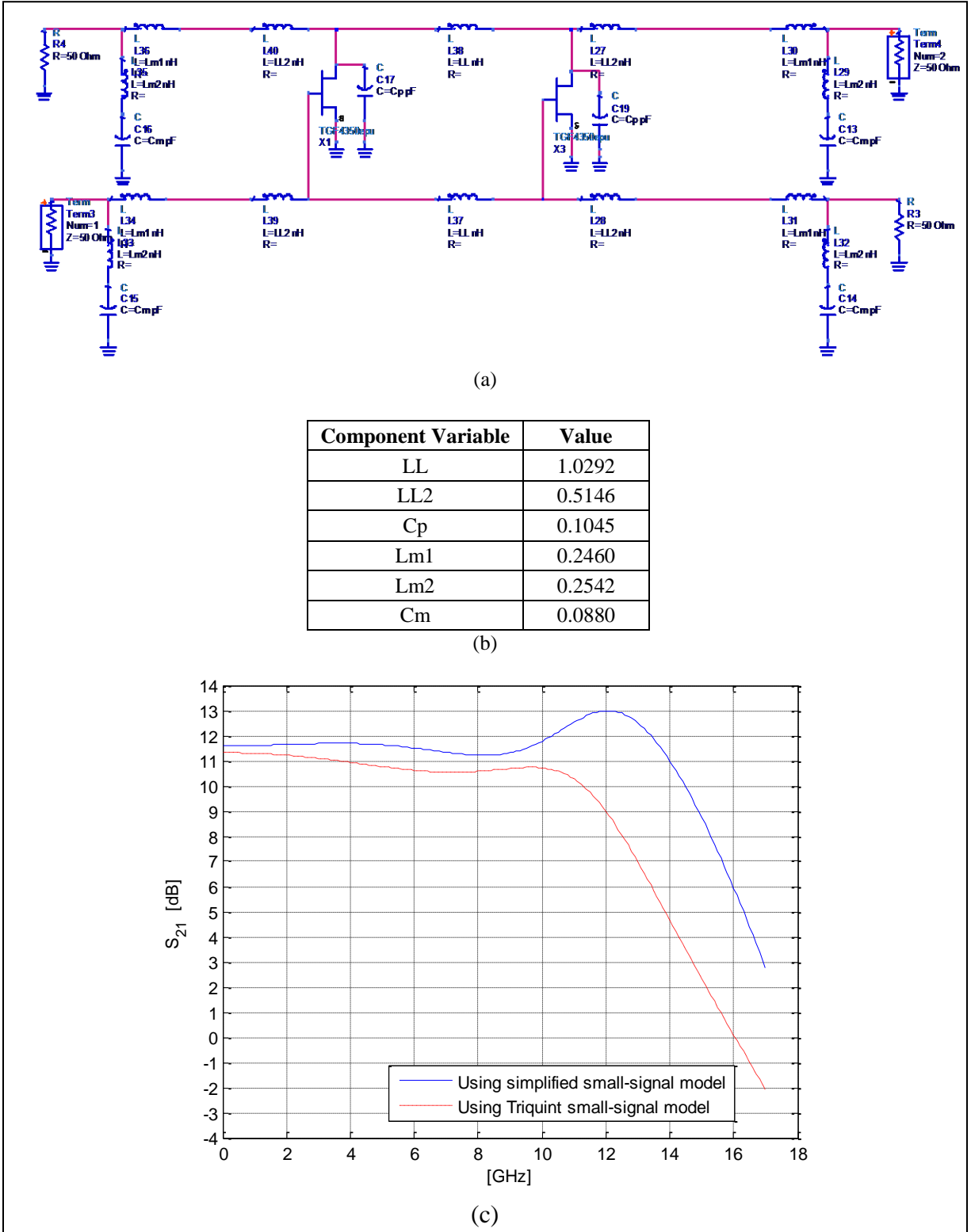


Figure C-6. (a) An example layout for $n = 2$ using lumped-elements, (b) component values, and (c) simulation results of lumped-element-based design.

INTENTIONALLY LEFT BLANK.

List of Symbols, Abbreviations, and Acronyms

3-D	three-dimensional
FDTD	finite-difference time-domain
MESFET	metal semiconductor field effect transistor
MoM	method-of-moments
MPIE	mixed potential integral equation
PCBs	printed circuit boards
RF	radio frequency
SPICE	Simulation Program with Integrated Circuit Emphasis
TE	transverse electric
TM	transverse magnetic

- 1 DEFENSE TECHNICAL
(PDF INFORMATION CTR
only) DTIC OCA
8725 JOHN J KINGMAN RD
STE 0944
FORT BELVOIR VA 22060-6218
- 12 US ARMY RSRCH LAB
ATTN IMAL HRA MAIL & RECORDS MGMT
ATTN RDRL CIO LL TECHL LIB
ATTN RDRL CIO LT TECHL PUB
ATTN RDRL SER U
TRAIAN DOGARU
KARL KAPPRA
DAHAN LIAO (3 COPIES)
ANTHONY MARTONE
GREGORY MAZZARO
KENNETH RANNEY
ANDY SULLIVAN
ADELPHI MD 20783-1197